EPR of Cr^{2+} in II-VI lattices

J. T. Vallin* and G. D. Watkins
General Electric Corporate Research and Development, P.O. Box 8, Schenectady, New York 12301
(Received 24 October 1973)

The EPR spectra of Cr^{2+} in cubic ZnS, ZnSe, ZnTe, and CdTe, and in hexagonal ZnS and CdS are reported. For each, $\Delta M = \pm 4, \pm 2, \pm 1$ transitions are observed allowing complete analysis of the $S=2$ spin Hamiltonian. A static tetragonal Jahn-Teller distortion is observed in all cases. Stress-alignment studies are described which allow a direct estimate of the Jahn-Teller coupling coefficients. From these, the magnitudes of the Jahn-Teller energies are estimated to be ~ 500 cm^{-1}. A ligand-field model is developed which satisfactorily accounts for the fine-structure parameters and their large variation from one crystal to another. In this treatment, ligand contributions to the spin-orbit interaction with excited d^4 terms are also included and found to be important. Strain-coupling coefficients, describing the changes in the fine-structure terms under externally applied stress, have been experimentally determined for CdTe (Cr^{2+}). A simple theory for this effect is developed which includes ligand contributions to the spin-orbit interactions but relies on point-ion estimates for the strain matrix elements. Agreement with experiment is reasonable for the tetragonal coefficients, but the wrong sign is predicted for the trigonal coefficients. The calculated trigonal coefficients for CdS do, however, satisfactorily account for the small departures from tetragonal symmetry observed in the spin Hamiltonian for Cr^{2+} in this hexagonal wurtzite lattice.

I. INTRODUCTION

The EPR spectra of Cr^{2+} in CdS [1-9] and ZnSe [10,11] have been reported earlier. From analysis of superhyperfine interactions with neighbors it was confirmed by these workers [2,4,10-12] that the chromium ion enters substitutionally into a cadmium (or zinc) atom lattice site. The anisotropic spectra were taken as evidence of a static Jahn-Teller distortion, but the precise nature of the distortion was given different interpretations. Estle *et al.*[2] interpreted the results to indicate a tetragonal distortion of the nearest neighbors. Morigaki,[3,4] on the other hand, postulated a substantial trigonal component to the distortion associated with motion of the central Cr^{2+} ion. Later far-infrared-absorption measurements[13] in ZnSe:Cr^{2+} were interpreted to indicate a pure tetragonal distortion.

The near-infrared absorption spectrum of Cr^{2+} has been studied[14-18] in most of the II-VI lattices (ZnS, ZnSe, ZnTe, CdS, CdSe, and CdTe). The spectra were found to be very similar in all cases. This was interpreted by Vallin *et al.*[14] to indicate that the ion suffers a static tetragonal Jahn-Teller distortion in all cases, and they interpreted the optical spectra accordingly, estimating the Jahn-Teller energy to be $\sim 400-600$ cm^{-1} for all II-VI lattices studied. The other authors,[15-18] however, have interpreted their optical-absorption results in terms of no Jahn-Teller coupling. A similar interpretation has been given by Nelkowski and Grebe[19] in their luminescence study of ZnS:Cr^{2+}.

The present study was undertaken to clarify the role and nature of the Jahn-Teller effect in these materials. We report here new EPR results for Cr^{2+} in ZnS, ZnSe, ZnTe, CdS, and CdTe. Preliminary reports of this work have been published elsewhere.[8,20]

Briefly our results are as follows. We find that a static Jahn-Teller distortion does indeed occur in all of the materials studied. The symmetry of the EPR spectrum reveals unambiguously that the distortion is a pure tetragonal one. The application of uniaxial stress to the crystal is found to produce substantial preferential alignment of the defects confirming that the distortion is Jahn-Teller in origin. These results are described in Sec. III along with the analysis of the EPR spectra. In Sec. IV a simple crystal-field theory for the electronic structure of the Cr^{2+} ion in a II-VI lattice is outlined including the theory of the Jahn-Teller effect. It is shown that the stress-alignment results can be analyzed to give a direct estimate of the Jahn-Teller coupling coefficients. This in turn is used to give an independent estimate of the Jahn-Teller energies. It is concluded that these estimates are generally consistent with those determined from the optical studies confirming the general interpretation of Vallin *et al.*[14]

In Sec. V we consider the theory of the spin Hamiltonian. Here we derive expressions for the contribution of spin-orbit and spin-spin interactions to the spin-Hamiltonian parameters and their dependence upon applied strain. These results are first evaluated within a simple point-ion approximation. The treatment is then expanded to include the effect of admixtures of the ligands into the wave functions of the central Cr^{2+} ion.

In Sec. VI we compare the theory with the experimental results. We conclude that the simple point-ion treatment is incapable of explaining the large variation of fine-structure parameters ob-

served in the various lattices. We find, however, that modest admixtures of the ligands are sufficient to provide a satisfactory explanation of the results. Attempts to match the measured strain-coupling coefficients (describing the strain dependence of the fine-structure splittings) are also described.

II. EXPERIMENTAL PROCEDURE

Most of the EPR studies were performed on a balanced bolometer system operating at 20 GHz. Limited measurements were also performed on a similar 14-GHz spectrometer whose magnetic-field range, normally 0–8 kG, was extended to 35 kG with a superconducting solenoid. For most of the experiments, magnetic-field modulation was employed with lock-in detection and recording, giving derivative of absorption spectra. For some experiments at 20 GHz, absorption spectra were also recorded directly by using modulation of the microwave power.[21]

The method of applying uniaxial stress to the crystals has been described previously.[22] Linewidth studies versus temperature in the range 4.2–14 °K were made by expelling the liquid helium and monitoring the temperature with a copper-constantan thermocouple as the microwave cavity warmed up. Studies in the range 14–20 °K were performed by pumping liquid hydrogen, the temperature being given by its vapor pressure.

Most of the samples studied were synthetic crystals into which chromium was introduced by diffusion. For this, a ~1-μm layer of metallic chromium was evaporated onto the sample surfaces and heated for several hours in quartz tubes sealed with ~$\frac{1}{3}$ atm of argon. Typical diffusion temperatures were CdTe (600 °C), ZnTe (750 °C), ZnSe (800 °C), and ZnS (1025 °C). The cubic crystals of each of these materials were grown in this laboratory by Woodbury, Swank, Aven, and Prener, respectively. The hexagonal ZnS crystal was obtained from the Eagle-Pitcher Company. The chromium-doped CdS sample was supplied to us by Locker of the Aerospace Research Laboratories and was originally grown from the vapor.

III. EXPERIMENTAL RESULTS

For all the II-VI materials studied, a complex anisotropic spectrum is observed at $\lesssim 4.2$ °K that we identify with Cr^{2+}. The spectrum in each case can be analyzed with the spin Hamiltonian

$$\mathcal{H} = \mu_B g_{\parallel} S_z H_z + \mu_B g_{\perp}(S_x H_x + S_y H_y) + DS_z^2 + E(S_x^2 - S_y^2) + \frac{F}{180}[35S_z^4 - 30S(S+1)S_z^2 + 25S_z^2] + \tfrac{1}{6}a(S_1^4 + S_2^4 + S_3^4), \quad (1)$$

where $\mu_B = e\hbar/2mc$ is the Bohr magneton, $\vec{H}$ is the magnetic field, and $S=2$. For the cubic materials (ZnS, ZnSe, ZnTe, CdTe), the x, y, z principal axes are found to coincide with the cubic (1, 2, 3) axes, with $E=0$, and the observed spectrum can be resolved into three identical equally intense spectra, each given by (1), but with the z axis of each along a different cubic axis (1, 2, 3). For the hexagonal materials (ZnS, CdS), *six* identical spectra are observed. The identification of the sets of axes in (1) for this case will be deferred until it is presented in detail.

For all cases observed, the dominant fine-structure term is D (i.e., $|D| \gg |a|, |E|, |F|$), and the general dependence of the $2S+1$ energy levels on applied magnetic field is therefore similar to that illustrated in Fig. 1. However, the form of the EPR spectrum observed depends strongly upon the size of D.

(i) If $|D| \gg h\nu_0$, where ν_0 is the spectrometer frequency, the observed transitions may be limited to the "forbidden" $M=+2 \rightleftharpoons -2$ and $M=+1 \rightleftharpoons -1$ ones, as shown by the short vertical solid lines in Fig. 1. If the magnetic field can be made large enough, however, the allowed $M=-1 \rightleftharpoons 0$ transition may also be observed, as shown.

(ii) If $|D| < h\nu_0$, many transitions will be observed. Shown in Fig. 1 by the vertical dashed lines are the allowed $\Delta M = \pm 1$ transitions where $h\nu_0 = 2.6|D|$.

The spectral transitions are relatively insensitive to the term in Eq. (1) involving F, which is small. The term was included in the analysis only for CdTe and ZnS, where a sufficient number of transitions were studied to allow its determination. For the other systems, analysis was performed assuming F to be zero.

A. CdTe

The spectrum observed at 4.2 °K, $\nu_0 = 20$ GHz, is shown for two different magnetic field orientations in Figs. 2(a) and 2(b). There are many lines spread over the full range of available magnetic field and a very complex angular dependence is observed. As previously mentioned, the spectrum can be resolved into three separate but identical spectra, each with its principal axis (z) along a different cubic axis. This is illustrated by the insets in the figure where the z axes of the three different orientations are labeled a, b, and c. The EPR lines associated with each orientation are correspondingly labeled on the recorded spectra.

With the magnetic field along a cubic axis [Fig. 2(a)], it is either parallel (defect a) or perpendicular (defects b, c) to the z axis and the energy levels of Fig. 1 apply directly. In fact, the specific values of a, F, E, and D used in the calculation of Fig. 1 are those which are the result of the analy-

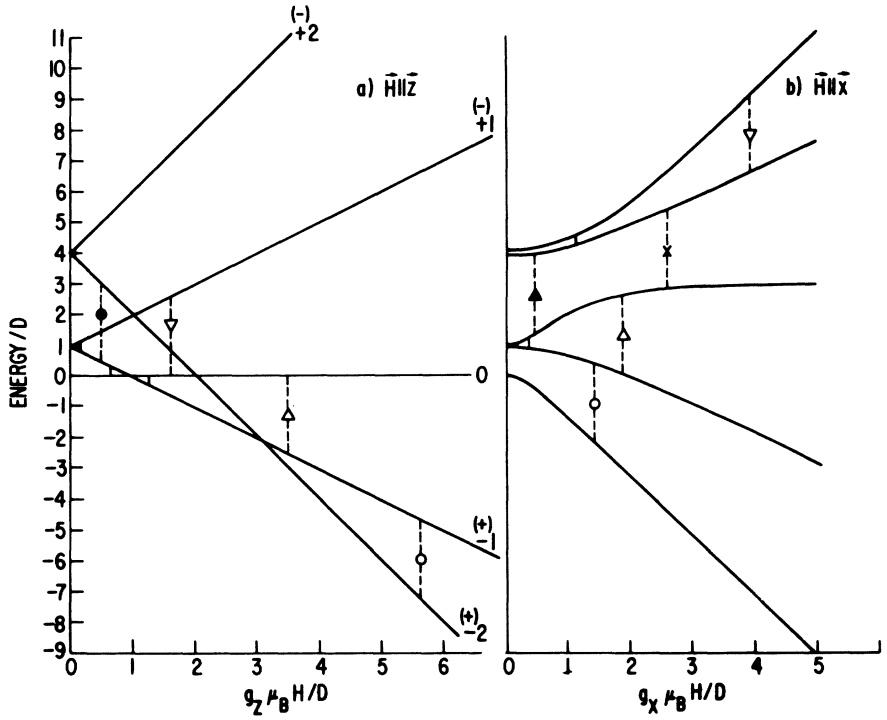

FIG. 1. Energy levels for Cr^{2+} ($S=2$) vs magnetic field given by Eq. (1) for $|D| \gg |a|$, $|E|$, $|F|$. The short solid vertical lines give the EPR transitions for $|D| \gg h\nu_0$. The vertical dashed lines are the allowed $\Delta M = \pm 1$ transitions for $h\nu_0 = 2.6|D|$. (Note that the ordinate is given in units of D, so that the figure applies for either sign of D. The M_s values are indicated for $D>0$. The values in brackets are for $D<0$.)

sis for Cr^{2+} in CdTe. In addition, the dashed lines correspond to the transitions for $h\nu_0/|D| = 2.6$, the value appropriate to Cr^{2+} in CdTe. Each spectral component in Fig. 2(a) is therefore also labeled to correspond with the transitions in Fig. 1.

The angular dependence of the spectrum for $\vec{H}$ in a {100} plane is summarized in Fig. 3, where the components from each of the differently oriented defects are displayed separately. The observed spectrum involves all three superposed. From Fig. 3, at $\psi = 45°$, the spectral lines in Fig. 2(b) can be identified, and they are also labeled accordingly.

Analysis was performed by a computer fit to the data of Fig. 3 and the results are shown by the solid lines. The spin Hamiltonian parameters deduced from this analysis are given in Table I. The sign of D was determined by the temperature dependence of the intensities of the spectral components in the range 1.5–4.2 °K. [For instance, the high-field line in Fig. 2(a) decreases in intensity as the temperature is lowered, the adjacent line increases. From Fig. 1 this gives the sign of D as positive.] The remaining signs are determined directly from the analysis.

We interpret the anisotropy in the spectrum to be evidence for a static Jahn-Teller distortion around the Cr^{2+} ion. Confirmation of this interpretation comes from the behavior under uniaxial stress, as shown in Fig. 2(c). We note that the relative intensities of the spectral components associated with the differently oriented defects change dramatically versus stress. Careful measurement of the integrated intensities reveals that the total intensity of the spectrum is constant and that the changes simply reflect redistribution among the three defect orientations. This easy reorientation at low temperatures confirms that the anisotropy does not result from a defect locked in the lattice nearby but rather must be an intrinsic property of the substitutional Cr^{2+} ion which is otherwise in the full tetrahedral symmetry (T_d) of the cadmium site which it occupies. The absence of an E term in the spin Hamiltonian, Eq. (1), reveals that the distortion must be a pure tetragonal one, the local symmetry being reduced from T_d to D_{2d}.

Studies with stress along the ⟨100⟩, ⟨110⟩, and ⟨111⟩ directions reveal that the degree of alignment is determined solely by the difference between the tetragonal components of strain e_θ along the z axis of each defect,[23] where, for the ith defect,

$$e_\theta^{(i)} = e_{zz}^{(i)} - \tfrac{1}{2}(e_{xx}^{(i)} + e_{yy}^{(i)}) \,. \tag{2}$$

Here the strains e_{ij} are defined in terms of the atomic displacements u_i in the usual manner:

$$e_{ij} = \frac{1}{2}\left(\frac{\partial u_i}{\partial x_j} + \frac{\partial u_j}{\partial x_i}\right) \,. \tag{3}$$

In Fig. 4 we summarize the stress-alignment results by plotting the ratio of the intensities of

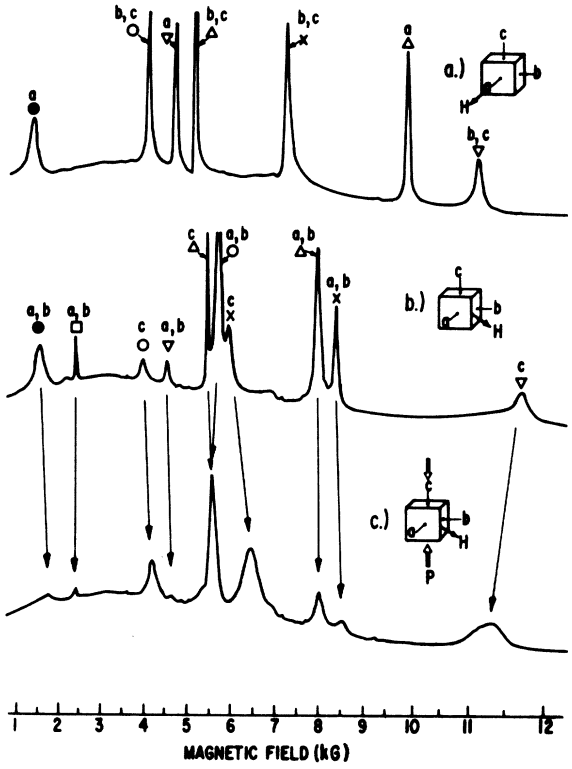

FIG. 2. EPR absorption spectrum for Cr^{2+} in CdTe at 4.2 °K, $\nu_0 = 20$ GHz: (a) $\vec{H} \| [100]$; (b) $\vec{H} \| [110]$; (c) $\vec{H} \| [110]$ and a compressional stress $\vec{P}$ of 75 kg/cm^2 parallel to the [001] direction. The lines are labeled to correspond to the transitions indicated in Fig. 1, the z axis associated with each line being donated by a, b, or c (see insets).

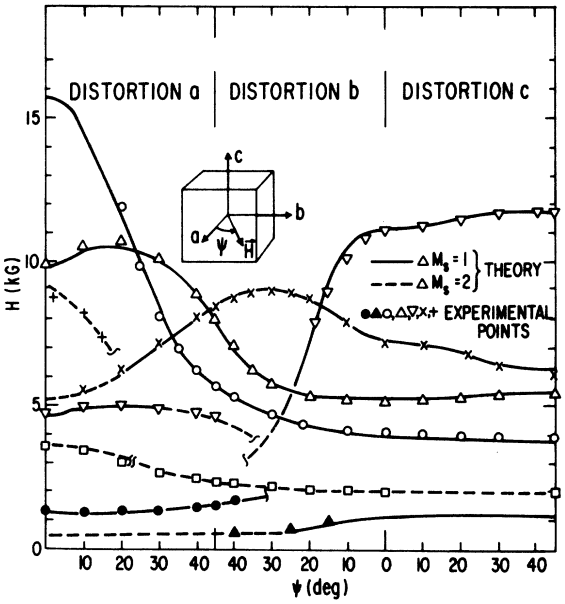

FIG. 3. Angular dependence of the CdTe : Cr^{2+} spectrum for $\vec{H}$ in the (001) plane. The components from each differently oriented defect are displayed separately.

the spectra associated with two orientations (c and a) versus the difference in the tetragonal strain components for each, $(e_\theta^c - e_\theta^a)$, resulting from the applied stress. For a stress along a cubic 3-axis (see insert in Fig. 4), the differences in e_θ are given by

$$e_\theta^c - e_\theta^a = e_\theta^c - e_\theta^b = \tfrac{3}{2}(e_{33} - e_{11}) = -\tfrac{3}{2}(S_{11} - S_{12})P(001), \tag{4}$$

where S_{11} and S_{12} are the elastic moduli (3.83×10^{-12} and -1.58×10^{-12} cm^2/dyne, respectively for CdTe)[24] and $P(001)$ is the applied pressure along the 3 axis. For stress along the $[0\bar{1}1]$ axis (see inset in Fig. 4), the differences are

$$e_\theta^c - e_\theta^a = e_\theta^b - e_\theta^a = \tfrac{3}{4}(e_{33} - e_{11}) = -\tfrac{3}{4}(S_{11} - S_{12})P(0\bar{1}1). \tag{5}$$

The results for both stress directions are identical and are plotted in Fig. 4(a) for 4.2 and 1.5 °K. At 1.5 °K, the alignment was still instantaneous on the time scale of our experiment ($\tau < 0.2$ sec) and

TABLE I. Spin Hamiltonian parameters for Cr^{2+} in II-VI crystals.

	CdTe	CdS	ZnTe	ZnSe	ZnS
$g_\parallel$	1.980 ± 0.015	1.934 ± 0.004	1.97 ± 0.01	1.961 ± 0.002	1.94 ± 0.02
$g_\perp$	1.980 ± 0.015	1.970 ± 0.004	1.99 ± 0.01	1.98 ± 0.02	1.98 ± 0.02
D (cm^{-1})	$+0.260 \pm 0.004$	-1.805 ± 0.005 [a]	$+2.30 \pm 0.02$ [a]	-2.48 ± 0.01 [b]	-1.86 ± 0.03
E (cm^{-1})	•••	$+0.0225 \pm 0.0010$	•••	•••	•••
a (cm^{-1})	$+0.05 \pm 0.01$	$+0.150 \pm 0.001$	$+0.140 \pm 0.007$	± 0.024 [c]	$+0.193 \pm 0.007$
F (cm^{-1})	-0.05 ± 0.02	•••	•••	•••	-0.14 ± 0.07
θ (deg)	•••	$+2.85 \pm 0.015$	•••	•••	•••

[a] This value, determined from the $M = 0 \rightleftharpoons \pm 1$ transition, is actually $D - \frac{2}{3}F$, and the indicated error strictly refers to the determination of this quantity. F is assumed zero in the analysis.

[b] This value, determined from the $M = \pm 1 \rightleftharpoons \pm 2$ transition observed by ir (Ref. 13), is actually $D + \frac{1}{9}F$. F is assumed zero in the analysis.

[c] Reference 10.

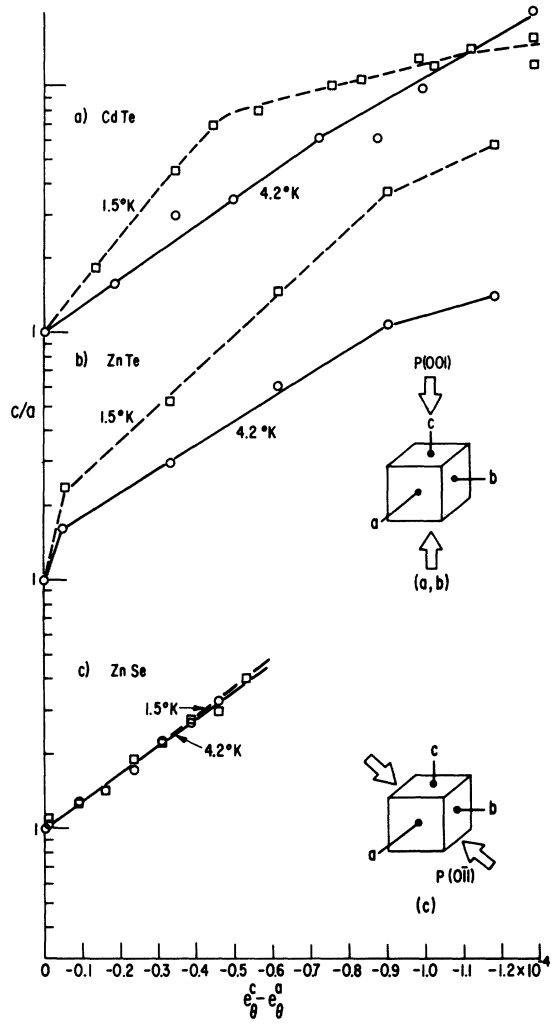

FIG. 4. Preferential alignment of the Jahn-Teller distortion direction vs applied tetragonal strain components for (a) CdTe, (b) ZnTe, and (c) ZnSe. The ordinate is the ratio of the intensity of the spectrum associated with orientation c to that of orientation a (see insets).

the kinetics of the reorientation process could therefore not be studied.

The EPR lines also shift in position significantly versus stress as can be seen in Fig. 2(c). A careful study of this effect was performed versus stress in the ⟨100⟩ and ⟨111⟩ directions and the results are shown in Figs. 5(a)–5(c). The stress and the magnetic-field geometry is shown in the inset of each figure. The broadening of the lines observed in Fig. 2(c) presumably results from inhomogeneity in the applied stress.

As the temperature is raised above ~8 °K, the linewidths are observed to broaden abruptly for all of the spectral components. In Fig. 6, we plot the log of the peak-to-peak derivative width of the $M=-1\rightleftharpoons 0$ transition for $\vec{H}$ parallel to the defect axis [transition Δ in Fig. 1(a)] versus $1/T$ in this region. At low temperatures, the absorption line is somewhat bell shaped, characteristic of an inhomogeneously broadened line, but in the high-temperature limit it has a Lorentzian shape, characteristic of lifetime broadening:

$$g(H)=\frac{2g\mu_B T_2/h}{1+[2\pi g\mu_B T_2(H-H_0)/h]^2}\ . \tag{6}$$

Making the simple assumption for analysis purposes that the inhomogeneous and Lorentzian contributions to the width simply add,[25] we may estimate the characteristic relaxation time T_2 versus temperature into the transition region as well, and these results are also given in Fig. 6. The data have been fit to the straight line

$$T_2^{-1}=(T_2)_0^{-1}\,e^{-E/kT}\ , \tag{7}$$

characteristic of a thermally activated process. In Table II we list the parameters for this fit. It should be noted, however, that the data are not accurate enough or over a large enough temperature range to distinguish between other possible dependences. For instance, it could also be fit to a T^3 dependence, also shown.

B. CdS

The EPR spectrum of Cr^{2+} has been the subject of study by a number of workers.[1–10] In these studies, only the $M=+2\rightleftharpoons -2$ transition was observed and from this it could be deduced only that D was negative and $|D|\gg h\nu_0$. To enhance the lines for study, these workers used a geometry to give the microwave magnetic field $\vec{H}_1\parallel\vec{H}$. None of the other transitions (Fig. 1) were observed and a direct measure of D and the other fine-structure terms in the $S=2$ Hamiltonian was therefore not possible.

Figure 7 shows the spectrum we observe at 20 GHz, 4.2 °K, with the conventional EPR geometry, $\vec{H}_1\perp\vec{H}$. In addition to most of the $M=+2\rightleftharpoons -2$ transitions, we observe a number of $M=+1\rightleftharpoons -1$ transitions and a transition at 14.2 kG which we identify as the $M=0\rightleftharpoons +1$ transition [see the short solid-line transitions in Fig. 1(a)]. The angular dependence of the spectrum with $\vec{H}$ in the $(11\bar{2}.0)$ plane is shown in Fig. 8. (The small splittings observed for some of the lines result from a slight misalignment, ~1°, of the crystal.)

CdS is hexagonal (wurtzite structure) with two inequivalent cadmium sites per unit cell.[26] Each site is surrounded by four sulfur atoms on the corners of a nearly regular tetrahedron. It is convenient therefore to express the spin Hamiltonian in terms of the (1, 2, 3) "cubic" axes associated with this tetrahedron. It can be considered a regular tetrahedron which has been compressed[26]

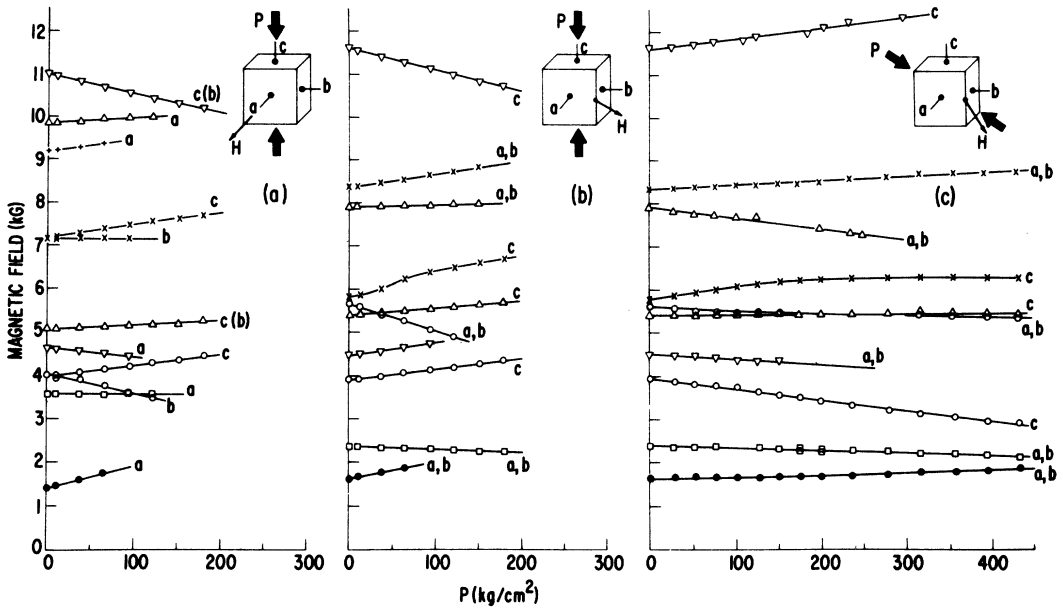

FIG. 5. Shifts of the CdTe:Cr^{2+} EPR lines vs applied uniaxial stress at 4.2 °K, $\nu_0 = 20$ GHz. The stress and magnetic field orientations are shown in the insets.

slightly (~0.6%) along the [111] axis. The two inequivalent sites share the same [111] compression axis which becomes the [000.1] c axis of the hexagonal crystal. The cubic axes associated with the two inequivalent sites can be transformed into each other by 180° rotation around the c axis. This is illustrated in Fig. 9 for one defect orientation associated with each inequivalent site.

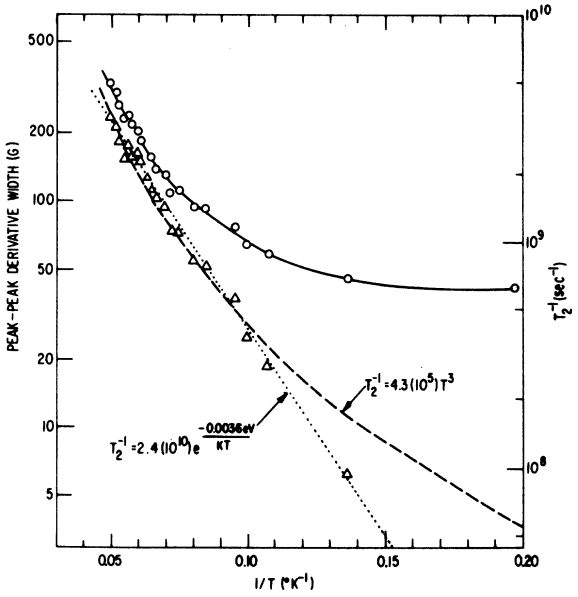

FIG. 6. Linewidth (peak-peak width of absorption derivative) (circled points) and T_2 (triangles) vs temperature for CdTe:Cr^{2+}. The line studied was the $M = -1 \rightleftharpoons 0$ transition with $\vec{H} \| \vec{z}$ [labeled Δ in Fig. 1(a)].

The presence of the two inequivalent sites for the Cr^{2+} ion doubles the number of lines observed in the spectrum over that for the cubic materials. However, one set of lines can be generated from the other by a 180° rotation around the c axis and contains no additional information. In Fig. 8 the transitions are indicated when the magnetic field is oriented along a specific defect principal axis, the labeling corresponding to the defect orientations of Fig. 9.

The results of analysis are given in Table I. (In this analysis, the frequency dependence of the $M = +2 \rightleftharpoons -2$ transitions determined by Estle *et al.*[2] was also used. F was assumed to be zero.) For each inequivalent site, there are three identical, equally intense spectra, each given by Eq. (1), but with the z axis of each oriented *approximately* (note the small angle θ, Fig. 9) along a different

TABLE II. Parameters for exponential fit to the temperature dependence of T_2.

Compound	Transition studied	$\vec{H}$ Orientation (x,y,z)	$(T_2^{-1})_0$ (sec^{-1})	E (eV)
CdTe	$-1 \rightleftharpoons 0$	(0,0,1)	$2.4(10^{10})$	0.0036
CdS[a]	$+2 \rightleftharpoons -2$		$[6.6(10^{11})]$	(0.0085)
ZnTe	$+1 \rightleftharpoons -1$	(1,0,0)	$6.3(10^{11})$	0.0063
		(0,0,1)	$12.6(10^{11})$	0.0063
ZnSe	$+1 \rightleftharpoons -1$	(1,0,0)	$5.5(10^{11})$	0.0085
ZnS	$+1 \rightleftharpoons -1$	(0,1,1)	$1.2(10^{11})$	0.0034

[a]Reference 9.

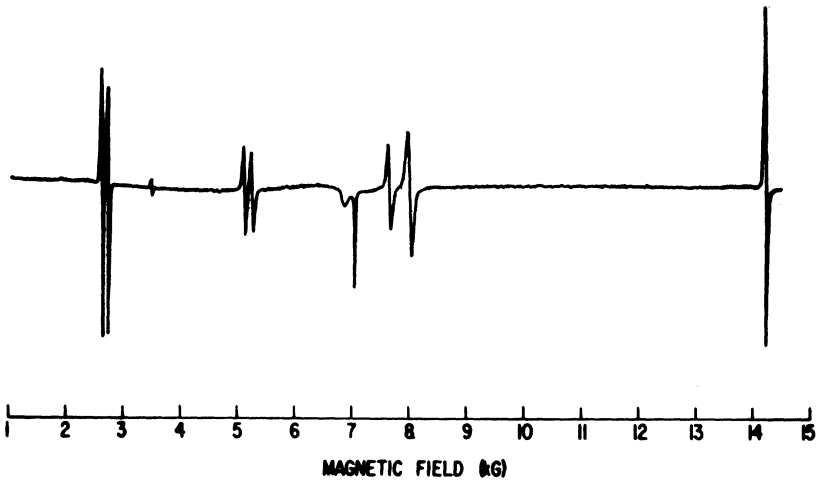

FIG. 7. EPR spectrum (absorption derivative) of CdS:Cr^{2+} at 4.2 °K, $\nu_0 = 20$ GHz. The magnetic field is in the $(11\bar{2}.0)$ plane and makes an angle (ψ) of 57.6° from the [000.1] c axis (see Fig. 8).

cubic axis (1, 2, 3). Again we interpret this to be the result of a static Jahn-Teller distortion as have previous workers.[1-9] The small values for E and θ suggest that, as in cubic CdTe, the distortion is primarily tetragonal in character (viewing this in terms of the normal distortion modes of a regular tetrahedron).

The EPR lines broaden as the temperature is raised.[1-9] A careful study of this has been performed by Wagner *et al.*[9] from 2 to 24 °K for the $M = +2 \rightleftharpoons -2$ transition and part of their results are shown by the dashed line in Fig. 10. They found that their data could be fit over the full temperature range to either

$$T_2^{-1} = 1.35 \times 10^3 T^5$$

or

$$T_2^{-1} = 5 \times 10^7 (e^{X_2} - 1)^{-1} + 1.2 \times 10^{12} X_1^{-7} J_6(X_1) ,$$

with $X_1 T = 150$ °K and $X_2 T = 3.8$ °K. [We note that over the limited range in T_2^{-1} studied by us in Fig. 10 the results of Wagner *et al.* could also be fit approximately to the simple exponential dependence

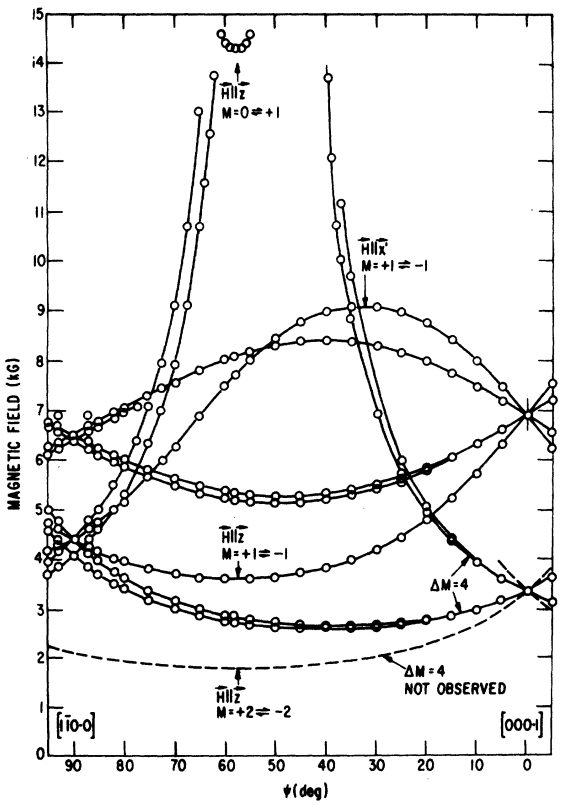

FIG. 8. Angular dependence of the CdS:Cr^{2+} spectrum in the $(11\bar{2}.0)$ plane. The dashed lines denote $\Delta M = 4$ transitions not observed in this study, but previously studied in Refs. 1-7.

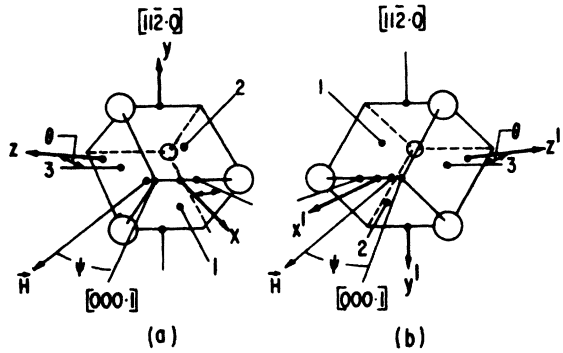

FIG. 9. Four nearest-neighbor sulfur atoms surrounding each of the two nonequivalent Cr^{2+} substitutional sites in CdS. Shown are the local "cubic" axes (1, 2, 3) and the principal axes (x, y, z or x', y', z') for one of the three Jahn-Teller distortion directions for each. One set of axes transforms into the other by a 180° rotation around the [000.1] c axis.

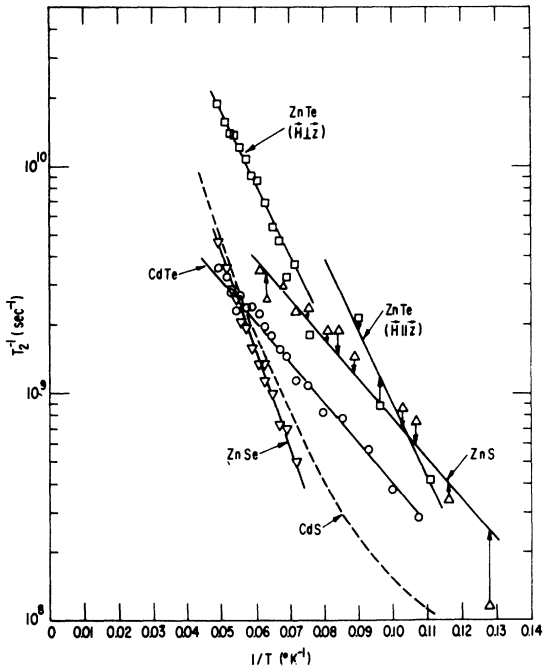

FIG. 10. Dependence of T_2 on temperature deduced from linewidth studies.

of Eq. (7) that we have used to analyze our results in the other II-VI materials. The results of such a fit are therefore also included in Table II for comparison purposes.]

The CdS crystals available to us were too small for studies versus stress. However, deWit *et al.*[10] have reported that stress produces alignment of the centers at 1.3 °K, which they interpret to confirm the interpretation as a Jahn-Teller distortion.

C. ZnTe

In the magnetic field range available in our 12-in. Varian electromagnet (0–15 kG), only the $M = +2 \rightleftharpoons -2$ and $M = +1 \rightleftharpoons -1$ transitions were observed. The angular dependence of these lines is similar to that for CdS (Figs. 7 and 8), with the exception that only one set of the three Jahn-Teller distorted spectra is observed because ZnTe is cubic. A computer fit to these transitions, observed both at 20 and 14 GHz, gives the spin-Hamiltonian parameters in Table I. The accuracy determined in this analysis is as indicated in the table, with the exception of that for D which is $\sim \pm 0.15$ cm^{-1}. The sign of D was determined from the temperature dependence of the intensities of the transitions in the range 1.5–4.2 °K.

To confirm the analysis, the magnetic field range was extended to 35 kG in a superconducting magnet. At the spectrometer frequency of 13.688 GHz, and $\vec{H} \parallel \langle 100 \rangle$, two additional intense lines were observed at 19.46 and 27.85 kG. We identify these as the allowed $M = 0 \rightleftharpoons -1$ transitions indicated in Fig. 1(a) (by the short vertical lines for the case $|D| > h\nu_0$). These allow the more accurate direct estimate of D indicated in the table. (See, however, footnote a in Table I.)

As was observed for CdTe, the application of uniaxial stress to the crystal produces preferential alignment among the three Jahn-Teller distortion directions, as evidenced by changes in the intensities of the corresponding spectral lines. The results for stress along a cube axis are given in Fig. 4(b) for measurements at 4.2 and 1.5 °K. [The tetragonal strain components were calculated from Eq. (4) with the elastic moduli S_{11} and S_{12} for ZnTe given by 2.40×10^{-12} and 0.873×10^{-12}, respectively.[24]] Again, the alignment appeared instantaneous ($\tau < 0.2$ sec) at 1.5 °K.

The $M = +1 \rightleftharpoons -1$ EPR lines were also observed to shift in position versus stress. Representative results for $\langle 110 \rangle$ stress are shown in Figs. 11(a) and 11(b). A detailed study versus stress orientation was not performed.

The EPR lines broaden abruptly as the temperature is raised above ~8 °K. Analysis similar to that described for CdTe (Fig. 6) gives the results in Table II and Fig. 10. Here the measurements were performed with $\vec{H} \parallel \langle 100 \rangle$ and the results are shown for the two $M = +1 \rightleftharpoons -1$ transitions: (a) $\vec{H} \perp \vec{z}$ and (b) $\vec{H} \parallel \vec{z}$. These two transitions span different ranges of T_2 because the static linewidth is much greater for (a) than (b). As analyzed, the two separate transitions give the same activation energy but their frequency factors differ by a factor of 2.

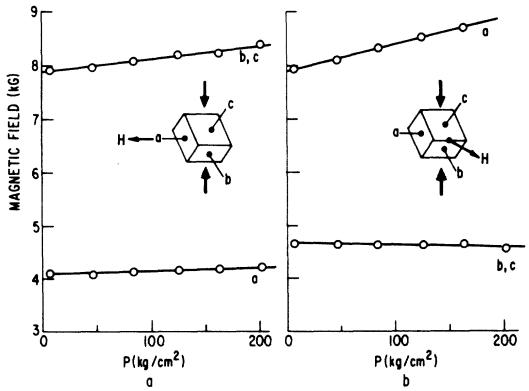

FIG. 11. Shifts in the EPR lines at 20 GHz for ZnTe: Cr^{2+} vs $\langle 110 \rangle$ compressional stress. The stress and magnetic-field orientations are indicated in the insets.

D. ZnSe

The $M=+2 \rightleftharpoons -2$ EPR transitions have been previously reported for Cr^{2+} in ZnSe by deWit *et al.*[10] and by Estle and Holton[11] and interpreted to indicate $|D| \gg h\nu_0$. In addition, a far-infrared absorption line at 7.43 ± 0.03 cm^{-1} has been observed by Vallin *et al.*[13] and identified as the $M=\pm 2 \rightarrow \pm 1$ transition in zero magnetic field. These results, coupled with the $M=+1 \rightleftharpoons -1$ transitions observed in our experiments, allow the analysis given in Table I. The sign of D was determined from the temperature dependence of the intensities of the transitions. The magnitude of a was too small to allow a determination of its sign.

Uniaxial stress produces alignment of the defects. The results at 1.5 and 4.2 °K for stress along a ⟨110⟩ axis are summarized in Fig. 4. Here the tetragonal strain components were calculated from Eq. (5) using the elastic moduli S_{11} and S_{12} for ZnSe given by 2.26×10^{-12} and 0.85×10^{-12} cm^2/dyn, respectively.[24] We note that the alignment is essentially independent of temperature.

The lines broaden for temperatures above ~12 °K and the results of a study in the range 14–20.4 °K are given in Table II and Fig. 10. Here the measurements were performed with $\vec{H} \parallel \langle 100 \rangle$ on the $M=+1 \rightleftharpoons -1$ transition $\vec{H} \perp \vec{z}$. The analysis was performed in the manner described for CdTe, using Eqs. (6) and (7).

E. ZnS

The spectra in cubic and hexagonal[27] ZnS, with the exception of the doubling of the lines in the hexagonal material (see discussion for CdS), appeared identical within the accuracy of the measurements. The lines were broader and substantially less intense in ZnS than in the other materials and slight differences would not have been detected. The $M=+2 \rightleftharpoons -2$ and $M=+1 \rightleftharpoons -1$ transitions were measured at 14 and 20 GHz. The low-field $M=0 \rightleftharpoons +1$ transition was observed at ~14.3 kG for $\nu_0=20$ GHz. In addition, a weak far-infrared–absorption line has been observed by Hughes and Vallin at 5.53 ± 0.10 cm^{-1} and identified as arising from $M=\pm 1 \rightleftharpoons \pm 2$ transition.[28] With this additional transition, F can also be estimated and the results of the analysis are summarized in Table I. The sign of D comes from the temperature dependence of the intensities from 1.5 to 4.2 °K.

The lines broaden as the temperature is raised above ~7 °K, and the results of the analysis are given in Table II and Fig. 10. In this study, $\vec{H} \parallel \langle 110 \rangle$ and the $M=+1 \rightleftharpoons -1$ transition, for which the defect z axis makes an angle of 45° with respect to $\vec{H}$, was observed.

Uniaxial stress produced only a relatively small effect on the intensities of the lines, with no apparent difference between 1.5 and 4.2 °K. Quantitative studies of the stress-induced alignment were therefore not possible. The apparent sign of the alignment was consistent with that found for the other materials (Fig. 4).

IV. ELECTRONIC STRUCTURE OF Cr^{2+} IN II-VI LATTICES

A. Theory

1. Point-ion crystal-field theory

In the crystal-field approximation one assumes that the host lattice is static and its effect on the Cr^{2+} ion can be simulated by an effective crystalline electrostatic potential.[29] In our treatment of Cr^{2+} we will assume that it is sufficient to consider the d^4 configuration and that the electronic states we study originate from the free-ion ^5D ground state. By symmetry, the tetrahedral (T_d) crystal field will split the ^5D term into an orbital doublet ^5E and an orbital triplet $^5T_2$. A calculation on a point-charge model with only nearest neighbors contributing to the crystal field gives for this splitting,

$$\Delta = \frac{20}{27} \frac{|eq_L|}{4\pi\epsilon_0 R} \frac{\langle r^4 \rangle}{R^4} \ . \tag{8}$$

Equation (8) is given in SI units, with ϵ_0 the vacuum dielectric constant, q_L the effective charge of the ligand ions, e the magnitude of the electron charge, R the nearest-neighbor distance, and $\langle r^n \rangle$ the average of r^n taken over the radial part of the Cr^{2+} wave function. For q_L negative, the $^5T_2$ state is predicted to be lowest in energy, as shown in Fig. 12.

2. Jahn-Teller coupling

If a crystalline defect has orbital degeneracy in the ground state then the system is unstable to at least one asymmetric displacement of the neighboring ions (the Jahn-Teller theorem).[30,31] For a defect with a T_2 orbital ground state in a crystal field of tetrahedral symmetry the possible asymmetric distortions have T_2 or E symmetry.[32] Our experimental results show that the distortions are of E symmetry, and we will therefore only treat these tetragonal distortions.

On symmetry grounds these distortions and their effects on the electronic states can be represented by the following equivalent operator[31]:

$$\mathcal{H}_D = V(Q_\theta \mathcal{E}_\theta + Q_\epsilon \mathcal{E}_\epsilon) + (\tfrac{1}{2}\kappa)(Q_\theta^2 + Q_\epsilon^2) \ . \tag{9}$$

In the first term of Eq. (9), the Jahn-Teller term, V is the coupling coefficient, Q_θ and Q_ϵ are normal coordinates of the nuclear displacements, and $\mathcal{E}_\theta$ and $\mathcal{E}_\epsilon$ are electronic operators having the following matrix representation with respect to the orbital T_2 functions of the ground state $(\Psi_\xi, \Psi_\eta, \Psi_\zeta)$[33]:

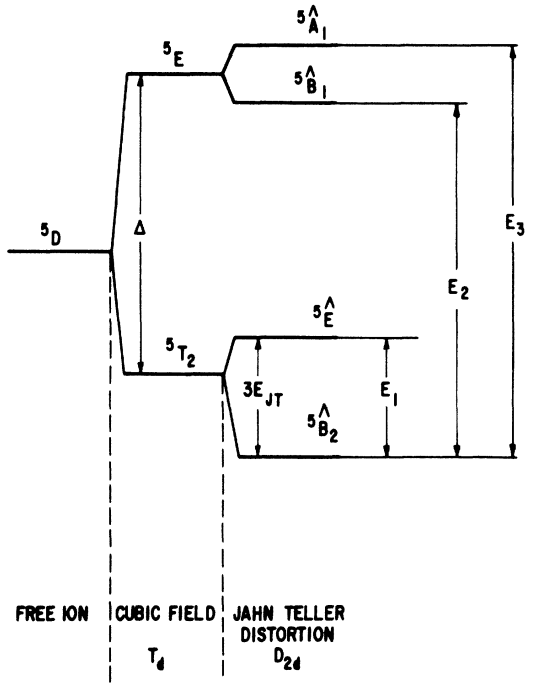

FIG. 12. Energy levels of $Cr^{2+}(3d^4)$ in a cation site of a II-VI material, showing the effect of a ⟨100⟩ tetragonal Jahn-Teller distortion.

$$\mathcal{E}_\theta=\begin{pmatrix}\frac{1}{2} & 0 & 0\\ 0 & \frac{1}{2} & 0\\ 0 & 0 & -1\end{pmatrix},\qquad \mathcal{E}_\epsilon=\begin{pmatrix}-\sqrt{3}/2 & 0 & 0\\ 0 & \sqrt{3}/2 & 0\\ 0 & 0 & 0\end{pmatrix}. \tag{10}$$

The second term represents the elastic energy associated with the distortion, κ being the force constant.

Because the operators $\mathcal{E}_\theta$ and $\mathcal{E}_\epsilon$ are diagonal in terms of the electronic states Ψ_ξ, Ψ_η, and Ψ_ζ, these states will also be eigenstates of $\mathcal{H}_D$ for arbitrary Q_θ and Q_ϵ.

For Ψ_ξ, Eq. (9) leads to a stable energy minimum in Q space at

$$Q_\theta = V/\kappa,\quad Q_\epsilon = 0\,, \tag{11}$$

which is a pure tetragonal distortion along the z axis. The energy at this distortion has been lowered by the Jahn-Teller energy

$$E_{JT} = V^2/2\kappa\,. \tag{12}$$

The local symmetry is reduced to D_{2d} and the ground state Ψ_ξ is of symmetry $^5\hat{B}_2$.[34] Ψ_ξ and Ψ_η remain degenerate, of symmetry $^5\hat{E}$, and are $3E_{JT}$ higher in energy, as shown in Fig. 12. The tetragonal distortion may also split the ^5E state, as shown.

There are three such stable distortions, corresponding to pure tetragonal distortions along each of the cubic axes. In the discussion to follow it will be convenient in each case to reserve the z axis for the distortion axis. Therefore, when it is necessary to distinguish the differently oriented distortions, we will label the distortion coordinates

$$Q_\theta^{(i)} = V/\kappa,\quad Q_\epsilon^{(i)} = 0\,, \tag{13}$$

where (i) labels the particular cubic axis (1, 2, 3) along which the tetragonal distortion has occurred.

Using the point-ion model for a T_d lattice, and considering nearest neighbors only, we obtain the following expression[35] for V:

$$V = (9/2\sqrt{2}\,R)(A+32B)\,, \tag{14}$$

where

$$A = \frac{16}{63}\,\frac{eq_L}{4\pi\epsilon_0 R}\,\frac{\langle r^2\rangle}{R^2}\,,\qquad B = \frac{10}{1701}\,\frac{eq_L}{4\pi\epsilon_0 R}\,\frac{\langle r^4\rangle}{R^4}\,. \tag{15}$$

B. Review of optical results

Optical absorption measurements on several II-VI compounds doped with chromium have been reported for the near-infrared region.[14–18] In all cases a broad absorption band (half-width ~400 cm^{-1}) centered around 5000 cm^{-1} has been observed. The interpretation of this band has been that it originates from transitions between the $^5T_2$ and ^5E manifold of states and the large width of the band indicates that the chromium ion couples strongly to the neighboring ions.

A zero-phonon line has also been observed in most cases. Its displacement from the peak of the broad band, and its relative intensity with respect to this band have been used by Vallin *et al.*[14] to estimate the Jahn-Teller energy and a characteristic average vibrational phonon energy $\hbar\bar{\omega}_E$ associated with the distortion. In this analysis it was concluded that consistent results could be obtained only if it was assumed that there was negligible Jahn-Teller coupling in the excited ^5E state. In this simple case, the Jahn-Teller energy in the ground state is equal to the displacement of the zero-phonon line, and its relative intensity, in turn, is given by

$$e^{-E_{JT}/\hbar\bar{\omega}_E}\,,$$

providing a direct estimate for $\hbar\bar{\omega}_E$.

In Table III we summarize the results of this analysis. We include also experimental estimates for the characteristic TA (L) lattice phonon in each material. This is the lowest-frequency (softest) critical-point phonon which has local E character at the metal-ion site, and would therefore be ex-

TABLE III. Results from optical absorption measurements[a] on chromium-doped II-VI crystals (in cm^{-1}).

Crystal	Δ	E_{JT}	$\hbar\bar{\omega}_E$	TA(L)[a]
ZnS	4650	575	91	72
ZnSe	4425	550(370)[b]	69(75)[b]	49
ZnTe	4460	535(360)[c]	67(65)[c]	42
CdS	4070	615	68	35
CdTe	4230	470	< 50	28

[a]Reference 14. [b]Reference 36. [c]Reference 37.

pected to dominate the average local tetragonal mode $\hbar\bar{\omega}_E$. The approximate agreement of the TA (L) mode frequency with $\hbar\bar{\omega}_E$ determined from the analysis of the optical spectra was taken by these workers as evidence that the model was substantially correct. In addition, observation in the far infrared of a transition within the $^5\hat{E}_2$ spin levels of ZnSe:Cr has been interpreted to supply confirmation that the distortion is a pure tetragonal one.[13]

More recently, Nygren and co-workers have reported a broad absorption band in the 500–2000-cm^{-1} region for ZnSe:Cr [36] and ZnTe:Cr [37] which they interpret in terms of a direct transition between the Jahn-Teller split states, $^5\hat{E}_2 \rightarrow {}^5\hat{E}$. Their analysis of these results give a Jahn-Teller energy of ~370 cm^{-1} and $\hbar\omega_E \sim 75$ cm^{-1} in ZnSe, and ~360 and ~65 cm^{-1}, respectively, in ZnTe. These are generally consistent with the other estimates and are also included in Table III.

The optical results therefore appear to find a consistent interpretation in terms of the following picture: In all II-VI lattices studied, the cubic-field splitting is ~4500 cm^{-1}, with the $^5T_2$ state lowest. A static tetragonal Jahn-Teller distortion occurs and the magnitude of the Jahn-Teller energy is roughly constant for all lattices at ~400–600 cm^{-1}.

However, other workers[15–19] have interpreted the spectra, not invoking the Jahn-Teller effect.

C. Results of present study

1. General conclusions

We interpret the anisotropy of the observed EPR spectra as unambiguous evidence for a static Jahn-Teller distortion for Cr^{2+} in all of the lattices studied. In the cubic materials, the axial symmetry ($E = 0$) along each of the three cubic axes indicates that the Jahn-Teller distortion is a pure tetragonal one. The small value of E in the hexagonal materials indicates that here too the distortion is primarily tetragonal. As discussed in Sec. IV B, the stress-alignment studies confirm this interpretation, ruling out the alternative possibility that the anisotropy reflects the presence of a defect locked in the lattice nearby.

2. Estimate of the Jahn-Teller coupling coefficient V

For the tetragonal mode of distortion, consider the displacement of the four nearest chalcogen neighbors (ligands) only:

$$Q_\theta = \frac{1}{\sqrt{2}\,R}\sum_{\alpha=1}^{4}\left[w_\alpha z_\alpha - \tfrac{1}{2}(u_\alpha x_\alpha + v_\alpha y_\alpha)\right], \tag{16}$$

where x_α, y_α, z_α are the coordinates of the αth neighbor and u_α, v_α, w_α, its displacement in the x, y, z directions, respectively. From (9), the effect of externally applied uniaxial stress can be written

$$\Delta E = -V\Delta Q_\theta, \tag{17}$$

where ΔQ_θ is the small additional component of mode Q_θ induced by the applied stress. Making the assumption that the ligands move under the applied stress in the same way as they would in the perfect lattice, Eq. (16) gives

$$\Delta Q_\theta = (2\sqrt{2}/3)\,\mathrm{Re}_\theta, \tag{18}$$

where e_θ is the bulk tetragonal strain given by Eq. (2).

At any Cr^{2+} site, the probability that the Jahn-Teller distortion will occur with its tetragonal axis (z axis) oriented along a specific cubic axis (i) is therefore proportional to the Boltzmann weighting factor

$$p^i \sim \exp(-\Delta E^i/kT) = \exp[(2\sqrt{2}/3)VRe_\theta^{(i)}/kT], \tag{19}$$

where $e_\theta^{(i)}$ is the component of tetragonal strain at the site defined along the ith axis.

If the externally applied stress is distributed uniformly throughout the crystal and random internal strains can be ignored, the relative intensities in the EPR spectrum for two different defect orientations, c and a, will therefore be given simply by

$$c/a = \exp[\delta(e_\theta^c - e_\theta^a)], \tag{20}$$

where

$$\delta = (2\sqrt{2}/3)VR/kT. \tag{21}$$

A simple exponential dependence upon applied strain is predicted with the slope δ (on a semilog plot) inversely proportional to temperature. From an experimental determination of the slope (Fig. 4), a direct estimate of the coupling coefficient can therefore be obtained.

If, however, internal strains (e_θ^{int}) or inhomogeneities in the applied strains (Δe_θ) are not negligible, i.e., if

$$\langle (e_\theta^{\mathrm{int}})^2\rangle^{1/2},\ \langle (\Delta e_\theta)^2\rangle^{1/2} \gtrsim \left|3kT/2\sqrt{2}\,VR\right|,$$

the simple relationship (20) will no longer hold. In this case, Eq. (19), properly normalized, would have to be averaged (convoluted) over the distributions of internal and inhomogeneous applied strain separately for c and a and then the ratio taken. The dependence of the intensity ratio c/a would then depend critically upon the specific distribution of strain. In general, it would not be exponential, and, in the limit of large internal strains, the temperature dependence would disappear.

In the data of Fig. 4, evidence of some of these difficulties is apparent. For ZnSe, an approximate exponential dependence is observed but with almost no temperature dependence between 4.2 and 1.5 °K. We interpret this as evidence of large internal strains,

$$\langle (e_\theta^{\rm int})^2 \rangle^{1/2} > |3kT/2\sqrt{2}\,VR| \ .$$

Consistent with this, the lines in this material are significantly broader than in ZnTe and CdTe.[38]

For ZnTe and CdTe, the lines are much sharper, indicating that internal strains are smaller. Consistent with this, the slopes in Fig. 4 are temperature dependent. They still scale by somewhat less than $1/T$, however, indicating residual effects of strain. In addition, evidence of inhomogeneity of applied stress is apparent in the broadening of the EPR lines under stress (Fig. 2). This presumably contributes to the observed departures from exponential dependence, particularly at high applied strains.

The data for CdTe are believed to be the most reliable. In this material the EPR lines were sharpest, indicating the smallest internal strains. Careful measurements of the integrated area of the spectral components were taken to obtain the data in Fig. 4. The values of δ were deduced from the initial (low applied strain) parts of the curves. The value of the coupling coefficient V was estimated using Eq. (21) from the results at 4.2 °K, where the effects of internal strains should be the least. The result is given in Table IV.

TABLE IV. Experimental estimates of the Jahn-Teller coupling coefficient (V) and Jahn-Teller energy (E_{JT}) from stress-alignment studies at 4.2 °K. Point-ion estimates of V are included for comparison. The Jahn-Teller energy was calculated from Eq. (12) using the characteristic tetragonal phonon energy $\hbar\bar{\omega}_E$ deduced from optical studies (Table III).

Lattice	$-V$(eV/Å) Expt.	Pt. ion	$\hbar\bar{\omega}_E$(cm^{-1})	E_{JT}(cm^{-1})
ZnSe	>0.40	0.37	69	>470
ZnTe	$\lesssim 0.32$	0.28	67	$\lesssim 200$
CdTe	$\lesssim 0.34$	0.21	(42)	$\lesssim 560$

Estimates for ZnTe and ZnSe are also included in the Table IV. For ZnTe, the initial jump at low stresses was disregarded and a best linear fit to the remainder of the curves was used to estimate δ.[39] Again, the value of V for each was estimated from the 4.2 °K data. Since the effect of internal strain is to reduce δ, the magnitude of V is always underestimated, as indicated. For ZnSe, the failure to see any temperature dependence means that the underestimate could be substantial, perhaps by a factor of 2 or more. For CdTe and ZnTe, however, the underestimate should not be great. In Table IV we give also the value predicted by the point-ion model, Eqs. (14) and (15). For this we have taken $q_L = -2e$[40] and have used the values of $\langle r^2 \rangle$ and $\langle r^4 \rangle$ calculated from Hartree-Fock wave functions for the Cr^{2+} ion, as tabulated by Abragam and Bleaney.[41] We note that the point-ion predictions are of the correct sign and roughly of the correct magnitude.

3. *Estimate of Jahn-Teller energy*

When the coupling coefficient V is known, it is possible to determine the Jahn-Teller stabilization energy from relation (12). An estimate of the force constant κ can be made from the relation

$$\kappa = \mu\bar{\omega}_E^2 \ , \tag{22}$$

where μ is an effective mass, and $\bar{\omega}_E$ is the characteristic frequency of the Jahn-Teller active modes. In our calculations we have used μ equals the ligand mass. The results are given in Table IV and are in reasonable agreement with the optical results. For CdTe we have used $\hbar\bar{\omega}_E$ equal to $\frac{3}{2}$ the energy of the Ta (L) phonon, which is consistent with the general trend in Table III.

4. *Linewidth versus temperature*

The fact that stress-induced alignment occurs "instantaneously" even at 1.5 °K suggests that the activation barrier for reorientation from one Jahn-Teller distortion direction to another must be very small. Therefore, as the temperature is raised, one would expect thermally activated reorientation to eventually become rapid enough to cause observable effects in the EPR spectrum itself. The broadening observed in the spectral lines at temperatures ~8–20 °K, Figs. 6 and 10, could be interpreted as evidence of this.

Thermally activated reorientation affects the linewidth in two different ways depending upon whether a spin flip is induced by the reorientation or not.

(i) If the spin does not flip, a reorientation simply shifts the resonance frequency as a result of the anisotropy of the spectrum. This random modulation of the resonance frequency is a pure T_2 process which initially causes a broadening,

but at higher temperatures produces a subsequent narrowing due to "motional averaging." When this occurs, an unambiguous identification of this effect is possible.[42]

(ii) If a spin flip occurs during reorientation, however, T_1 is also affected. In this case, the initial broadening is the same but motional averaging may not be observed. In this case, it is difficult to distinguish this mechanism from other possible T_1 mechanisms.

In no case was motional averaging of the Cr^{2+} spectrum observed. In fact, observation with $\vec{H} \parallel \langle 111 \rangle$, where reorientation produces no changes in the static spectrum, also reveals broadening in approximately the same temperature region. From this we conclude that the broadening is a T_1 process. Whether this results from reorientation or some other process therefore cannot be unambiguously determined. If this does result from reorientation, the activation energies deduced in Table II would be identified with the barrier height for reorientation. These low activation energies are generally consistent with the observation of stress-induced alignment at 1.5 °K.

V. THEORY OF THE SPIN HAMILTONIAN

A. Fine structure

Due to the local electronic symmetry the effective spin Hamiltonian for the ground state has to have the following form:

$$\mathcal{H}_s = DS_z^2 + E(S_x^2 - S_y^2) + \tfrac{1}{180}F\,[35S_z^4 - 30S(S+1)S_z^2 + 25S_z^2] + \tfrac{1}{6}a(S_1^4 + S_2^4 + S_3^4)\,, \tag{23}$$

where $E = 0$ in D_{2d} symmetry.

These fine-structure terms arise from spin-orbit and spin-spin interactions which serve to couple the spin to the spatial parts of the wave function. Within a manifold of states derived from a single LS term (^5D in our case), the first-order spin-orbit and spin-spin terms can be represented by the equivalent operators[43]

$$\mathcal{H}_{so} = \lambda \vec{L} \cdot \vec{S}\,, \tag{24}$$

$$\mathcal{H}_{ss} = -\rho[(\vec{L}\cdot\vec{S})^2 + \tfrac{1}{2}\vec{L}\cdot\vec{S} - \tfrac{1}{3}\vec{L}^2\vec{S}^2 \tag{25a}$$

$$= -\rho[\tfrac{2}{3}(L_\theta S_\theta + L_\epsilon S_\epsilon) + \tfrac{1}{2}(L_\xi S_\xi + L_\eta S_\eta + L_\zeta S_\zeta)]\,, \tag{25b}$$

where

$$L_\theta = L_z^2 - \tfrac{1}{2}(L_x^2 + L_y^2)\,,$$
$$L_\epsilon = \tfrac{1}{2}\sqrt{3}\,(L_x^2 - L_y^2)\,, \tag{26}$$
$$L_\xi = L_y L_z + L_z L_y\,,$$

with obvious changes for L_η and L_ζ and with corresponding definitions for S_θ, S_ϵ, S_ξ, S_η, and S_ζ. Here matrix elements of $\vec{L}$ and $\vec{S}$ are those of the standard angular-momentum operators within the $|L, M_L, S, M_s\rangle$ manifold.

In a simple crystal-field treatment where the wave functions are taken to be those of the free ion, a single parameter each for λ and ρ is sufficient for all matrix elements within the term. This approximation is often made in the EPR literature and found to give satisfactory results. However, in a more general treatment (ligand field) where the wave functions are not so constrained, this is no longer true. In this more general case, the Wigner-Eckart theorem[44] says only that there is a single multiplicative parameter (reduced matrix element) for each set of matrix elements $\langle \Gamma^a | \Gamma^b | \Gamma^c \rangle$ where the initial and final states transform as Γ^a and Γ^c and the interaction as Γ^b.

In our treatment we will consider the problem as a small distortion from cubic (T_d) symmetry. We will allow full generality for the undistorted T_d case but will not consider the wave functions as significantly altered as a result of the Jahn-Teller distortion. Since $\vec{L}$ transforms as T_1, there are, therefore, two reduced matrix elements for the spin-orbit interaction:

$$\lambda_1 = \langle T_2 | \, | \mathcal{H}_{so} | \, | T_2 \rangle\,, \qquad \lambda_2 = \langle T_2 | \, | \mathcal{H}_{so} | \, | E \rangle\,. \tag{27}$$

For the spin-spin interaction, there are three reduced matrix elements:

$$\rho_1 = \langle T_2 | \, | \mathcal{H}_{ss}^{(T_2')} | \, | T_2 \rangle\,, \qquad \rho_2 = \langle T_2 | \, | \mathcal{H}_{ss}^{(T_2')} | \, | E \rangle\,, \qquad \rho_3 = \langle T_2 | \, | \mathcal{H}_{ss}^{(E)} | \, | T_2 \rangle\,. \tag{28}$$

Here the notation $\mathcal{H}_{ss}^{(E)}$ refers to the first term in (25b), for which the orbital parts transform as E, and $\mathcal{H}_{ss}^{(T_2')}$ refers to the second term for which the orbital parts transform as T_2.

With these spin-orbit and spin-spin parameters, we find to second order in λ and first order in ρ,

$$D = \lambda_1^2/E_1 - 4\lambda_2^2/E_2 - 3\rho_3\,, \tag{29}$$

and to order λ^4, $\rho\lambda^2$, and ρ^2,

$$a = (36/E_1^2 E_3)[\rho_2^2 E_1^2 + 2\lambda_1\lambda_2\rho_2 E_1 + \lambda_1^2\{\lambda_2^2 + \tfrac{1}{2}(\rho_1 + \rho_3)E_3\}]\,. \tag{30}$$

E_1, E_2, and E_3 are defined in Fig. 12.

It has been demonstrated[45] that spin-orbit coupling between different LS terms provides an additional interaction which can be expressed as an effective Hamiltonian in the ground term of exactly the same form as the spin-spin interaction, Eq. (25), when this coupling is treated by second-order perturbation theory. The ρ_i's thus can be considered to represent the combined effect of the

true spin-spin interaction and the spin-orbit interaction to the higher LS terms of the d^4 configuration having $S=1$. [This is strictly correct only for D in Eq. (29). The terms involving ρ in the expression for a, Eq. (30), which are obtained by second- and third-order treatments in the ground manifold are not fully equivalent to a full fourth-order calculation to the excited triplet states. However, Eq. (30) should represent a reasonable approximation to these terms.]

In the Appendix we show that an estimate of those parts of ρ_1, ρ_2, and ρ_3 arising from the spin-orbit coupling to the triplet states can be made by simply assuming the excited states all to lie at a large energy E above the ground state. The result is

$$\begin{aligned}\rho_1 &= (5/9E)(\lambda_1^2+2\lambda_2^2)+\rho_{10}\,,\\ \rho_2 &= (5/3E)\lambda_1\lambda_2+\rho_{20}\,,\\ \rho_3 &= (5/9E)(-\lambda_1^2+4\lambda_2^2)+\rho_{30}\,,\end{aligned} \tag{31}$$

where ρ_{10}, ρ_{20}, and ρ_{30} represent the true spin-spin interaction. A check on this simple procedure is available for the free ion. For it, $\lambda_1=\lambda_2=\lambda$, $\rho_{10}=\rho_{20}=\rho_{30}=\rho_0$, giving

$$\rho=\rho_1=\rho_2=\rho_3=5\lambda^2/3E+\rho_0\quad. \tag{32}$$

With $\lambda=57$ cm^{-1},[14] $E\cong 20\,000$ cm^{-1},[46] and $\rho_0=0.12$ cm^{-1},[41] we obtain

$$\rho=0.42\ \text{cm}^{-1}\,,$$

in good agreement with the value deduced from spectroscopic free-ion energies by Pryce[47] of 0.42 ± 0.04 cm^{-1}. This demonstrates the important fact that the spin-orbit coupling to the excited triplet states provides the dominant contribution to ρ (~ 0.3 cm^{-1}), the true spin-spin interaction being relatively less important (~ 0.1 cm^{-1}).[48] This has important consequences for the cubic field term a.

Substituting (31) into (30), we obtain

$$\begin{aligned}a=\frac{36\lambda_1^2\lambda_2^2}{E_1^2E_3}&\left[1+\frac{5}{3}\left(\frac{2E_1+E_3}{E}\right)+\left(\frac{5E_1}{3E}\right)^2\right]\\ &+\frac{36}{E_1^2E_3}\left[\rho_{20}^2E_1^2+2\lambda_1\lambda_2\rho_{20}E_1\left(1+\frac{5E_1}{3E}\right)\right.\\ &\left.+\tfrac{1}{2}\lambda_1^2(\rho_{10}+\rho_{30})E_3\right].\end{aligned} \tag{33}$$

We note that, to the extent that the second term involving the true spin-spin terms is small, the cubic field varies as $\sim\lambda_1^2\lambda_2^2$.

B. External perturbations

1. *Magnetic field*

The Zeeman term $\mathcal{H}_Z$, in the effective Hamiltonian for the ground state must, according to group theory, have the following form (for D_{2d} symmetry):

$$\mathcal{H}_Z=\mu_B[g_\parallel S_z H_z+g_\perp(S_xH_x+S_yH_y)]\,, \tag{34}$$

where $\mu_B=e\hbar/2mc$ is the Bohr magneton and $\vec{H}$ is the magnetic field. With the perturbing Hamiltonian

$$\lambda\vec{L}\cdot\vec{S}+\mu\vec{L}\cdot\vec{H}+g_0\mu_B\vec{S}\cdot\vec{H}\,,$$

second-order perturbation gives, for the terms linear in the spin-orbit interaction,

$$g_\parallel=g_0-8\lambda_2k_2/E_2\,,\quad g_\perp=g_0-2\lambda_1k_1/E_1\,, \tag{35}$$

where g_0 ($=2.0023$) is the free-electron g factor. Here, in analogy to λ_1 and λ_2,

$$\begin{aligned}k_1\mu_B=\mu_1&=\langle T_2||\mathcal{H}_{LH}||T_2\rangle\,,\\ k_2\mu_B=\mu_2&=\langle T_2||\mathcal{H}_{LH}||E\rangle\end{aligned} \tag{36}$$

are defined in terms of the reduced matrix elements μ_1 and μ_2 for the orbital Zeeman interaction $\mu\vec{L}\cdot\vec{H}$.

2. *Static strain*

An applied stress will also give changes $\mathcal{H}_e$ in the spin Hamiltonian. For the D_{2d} symmetry, these changes can be written

$$\begin{aligned}\mathcal{H}_e=c_1e_1S_\theta+c_2e_\theta S_\theta+c_3e_\epsilon S_\epsilon\\ +c_4e_\zeta S_\zeta+c_5(e_\xi S_\xi+e_\eta S_\eta)\,.\end{aligned} \tag{37}$$

Here, the strain components (e_i) and spin operators (S_i) are defined in the same manner as the orbital angular momentum operators (L_i) in Eq. (26). In addition,

$$e_1=e_{xx}+e_{yy}+e_{zz}\,.$$

We have estimated the constants $c_1,\cdots,c_5$ using third-order perturbation theory (first order in strain and second order in spin-orbit interaction) and obtain the following results:

$$\begin{aligned}c_1&=(16\lambda_2^2/E_2^2)(T_2-T_1)\,,\\ c_2&=(8\lambda_2^2/E_2^2)(U_2-U_1)+(3\lambda_1^2/E_1^2)U_1\,,\\ c_3&=-(3\lambda_1^2/E_1^2)U_1\,,\\ c_4&=(3\lambda_1^2/E_1^2)W_1+(12\lambda_1\lambda_2/E_1E_3)W_2\,,\\ c_5&=(6\lambda_2^2/E_1E_2+3\lambda_1^2/E_1^2)W_1+(6\lambda_1\lambda_2/E_1E_2)W_2\,.\end{aligned} \tag{38}$$

λ_1 and λ_2 are given by Eq. (27), and we will now introduce the reduced matrix elements T, U, and W. The matrix elements of the crystal field produced by the strain (within the ^5D manifold of states) can be expressed by the matrix elements of the following equivalent operator (in T_d symmetry):

$$\begin{aligned}\mathcal{H}_{eL}=Te_1L^2+U(e_\theta L_\theta+e_\epsilon L_\epsilon)\\ +W(e_\xi L_\xi+e_\eta L_\eta+e_\zeta L_\zeta)\,.\end{aligned} \tag{39}$$

By symmetry there are six different reduced matrix elements for T, U, and W,

$$T_1=\langle T_2||\mathcal{H}_{eL}^{(A1)}||T_2\rangle,\quad T_2=\langle E||\mathcal{H}_{eL}^{(A1)}||E\rangle,$$
$$U_1=\langle T_2||\mathcal{H}_{eL}^{(E)}||T_2\rangle,\quad U_2=\langle E||\mathcal{H}_{eL}^{(E)}||E\rangle, \tag{40}$$
$$W_1=\langle T_2||\mathcal{H}_{eL}^{(T2)}||T_2\rangle,\quad W_2=\langle T_2||\mathcal{H}_{eL}^{(T2)}||E\rangle,$$

where $\mathcal{H}_{eL}^{(A1)}$, $\mathcal{H}_{eL}^{(E)}$, and $\mathcal{H}_{eL}^{(T2)}$ refer to the first, second, and third terms, respectively, of Eq. (39).

The reduced matrix elements T, U, and W have been calculated from the point-ion model considering nearest neighbors only.[49] The results are

$$T_2-T_1=-35B,$$
$$U_1=-A-32B,\quad U_2=-A+24B, \tag{41}$$
$$W_1=A+120B,\quad W_2=A-90B.$$

A and B are given by Eq. (15).

C. Ligand effects

In this section we will consider the effect of admixtures of ligand p functions into the central (Cr^{2+}) ion d functions. There will be symmetry limitations on the linear combinations of ligand orbitals and the possible combinations of interest to us are given in Table V together with the central-ion wave functions. The coordinate system and the numbering used are shown in Fig. 13.

We can now write the one-electron orbitals for the central ion, including their mixing with ligand orbitals, in the following way:

$$\psi_\theta=N_E(d_\theta+\alpha\pi_\theta),$$
$$\psi_\xi=N_{T2}(d_\xi+\beta\sigma_\xi+\gamma\pi_\xi), \tag{42}$$

with obvious changes for ψ_ϵ, ψ_η, and ψ_ζ.

1. Spin-orbit matrix elements

To evaluate the spin-orbit matrix elements, we take

$$\mathcal{H}_{so}=\lambda\vec{L}\cdot\vec{S}=\sum_i\zeta\vec{l}_i\cdot\vec{s}_i, \tag{43}$$

where the summation is over the $i=4$ electrons and ζ is the effective one-electron spin-orbit parameter.

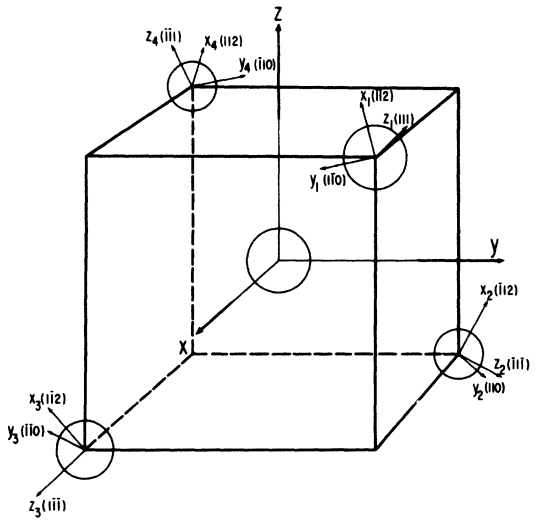

FIG. 13. Coordinate axes for the central-ion and ligand orbitals, after Viste and Gray (Ref. 52).

This can be further expanded as

$$\mathcal{H}_{so}=\sum_{\mu,i}\zeta^\mu\vec{l}_i(\mu)\cdot\vec{s}_i, \tag{44}$$

where the summation is over the $\mu=5$ central plus four nearest ligand ions. ζ^μ is the one-electron spin-orbit constant appropriate for the μth ion and $\vec{l}_i(\mu)$, the orbital angular momentum operator centered at its origin. With the molecular orbitals of Eq. (42), this leads directly to the reduced matrix elements

$$\lambda_1=\tfrac{1}{4}\zeta_1=\langle T_2||\mathcal{H}_{so}||T_2\rangle$$
$$=\tfrac{1}{4}N_{T_2}^2[\zeta^d+\gamma(\sqrt{2}\,\beta-\tfrac{1}{2}\gamma)\zeta^x],$$
$$\lambda_2=\tfrac{1}{4}\zeta_2=\langle T_2||\mathcal{H}_{so}||E\rangle \tag{45}$$
$$=\tfrac{1}{4}N_{T_2}N_E[\zeta^d+\alpha(\beta/\sqrt{6}+\gamma/2\sqrt{3})\zeta^x].$$

In deriving these results, we have neglected, as small, matrix elements of $\mathcal{H}_{so}$ between orbitals centered on different ions. Here

TABLE V. Basis functions for a T_d complex.[a]

Irreducible representation	Ligand p orbitals: σ orbitals	Ligand p orbitals: π orbitals	Metal orbitals
A_1	$\frac{1}{2}(z_1+z_2+z_3+z_4)$		
E_θ		$\frac{1}{2}(x_1-x_2-x_3+x_4)$	d_θ
E_ϵ		$\frac{1}{2}(y_1-y_2-y_3+y_4)$	d_ϵ
$T_{2\xi}$	$\frac{1}{2}(z_1-z_2+z_3-z_4)$	$\frac{1}{4}[x_1+x_2-x_3-x_4-\sqrt{3}\,(y_1+y_2-y_3-y_4)]$	d_ξ
$T_{2\eta}$	$\frac{1}{2}(z_1+z_2-z_3-z_4)$	$\frac{1}{4}[x_1-x_2+x_3-x_4+\sqrt{3}\,(y_1-y_2+y_3-y_4)]$	d_η
$T_{2\zeta}$	$\frac{1}{2}(z_1-z_2-z_3+z_4)$	$-\frac{1}{2}(x_1+x_2+x_3+x_4)$	d_ζ

[a]Referred to the coordinate system shown in Fig. 13.

$$N_{T_2} = (1+\beta^2+\gamma^2+2\beta\langle d_\xi|\sigma_\xi\rangle+2\gamma\langle d_\xi|\pi_\xi\rangle)^{-1/2},$$
$$N_E = (1+\alpha^2+2\alpha\langle d_\theta|\pi_\theta\rangle)^{-1/2}, \quad (46)$$

with $\langle i|j\rangle$ denoting the overlap integral between the corresponding orbitals.

Because the ligand spin-orbit constant ζ^x is often much larger than that of the central ion ζ^d, even small admixtures (α, β, and γ) of ligand wave functions may have significant effects on λ_1 and λ_2. In particular, λ_1 and λ_2 are no longer equal.

2. *Orbital angular momentum matrix elements*

For the free-ion d functions, the reduced matrix elements μ_1, μ_2 of the Zeeman-orbit interaction, Eq. (36), are equal to μ_B ($=e\hbar/2mc$), i.e., $k_1 = k_2 = 1$. For the ligand-admixed orbitals, k_1 and k_2 are therefore given by

$$k_1 = \langle\psi_\xi|l_z|\psi_\eta\rangle\langle d_\xi|l_z|d_\eta\rangle,$$
$$k_2 = \langle\psi_\epsilon|l_z|\psi_\zeta\rangle/\langle d_\epsilon|l_z|d_\zeta\rangle, \quad (47)$$

and are often referred to as "orbital reduction factors."[50]

Proceeding as in Sec. V C 1, but including here matrix elements between orbitals centered on the central ion and the ligands (but excluding ligand-ligand terms), we obtain

$$k_1 = N_{T_2}^2(1-\tfrac{1}{2}\gamma^2+\sqrt{2}\,\beta\gamma + 2\beta\langle d_\xi|\sigma_\xi\rangle+2\gamma\langle d_\xi|\pi_\xi\rangle),$$
$$k_2 = N_{T_2}N_E(1+\alpha\gamma/2\sqrt{3}+\alpha\beta/\sqrt{6}+\alpha\langle d_\theta|\pi_\theta\rangle + \beta\langle d_\xi|\sigma_\xi\rangle+\gamma\langle d_\xi|\pi_\xi\rangle). \quad (48)$$

VI. DISCUSSION

A. Fine-structure constants

Using the point-ion model with the free-ion values for λ ($=57$ cm^{-1}) and ρ ($=0.42$ cm^{-1}) and the experimental optical data for E_1 and E_2, we may calculate D from Eq. (29), and a from Eq. (30). We obtain $D \cong -1.6$ cm^{-1} and $a \cong 0.05$ cm^{-1} for all the crystals in this study. The experimental values of D for ZnS and CdS (Table I) are in favorable agreement with the point-ion predictions. However, for ZnSe the agreement is poor and for ZnTe and CdTe even the wrong sign for D is predicted. The experimental a values differ considerably from compound to compound, although the values for ZnS and CdS are quite similar. These large discrepancies between theory and experiment show that the point-ion model is insufficient to describe the fine structure of Cr^{2+} in II-VI compounds.

Now consider the effect of ligand admixtures into the central-ion wave functions. In order to be able to use Eq. (45) we must first estimate the coefficients α, β, and γ. For this, we proceed as follows.

(i) We take α, β, and γ as proportional to the negative of the corresponding group overlap integrals, i.e.,

$$\alpha = -k_0\langle d_\theta|\pi_\theta\rangle,$$
$$\beta = -k_0\langle d_\xi|\sigma_\xi\rangle, \quad (49)$$
$$\gamma = -k_0\langle d_\xi|\pi_\xi\rangle.$$

The rationale for this is twofold. In the first place, orthogonalization of the central-ion and ligand functions alone produces admixtures according to (49). Second, covalency produces additional contributions, which, in the Wolfsberg-Helmholz approximation[51] to the relevant matrix elements, are also proportional to the negative of the group overlaps.

(ii) As a rough guide for these overlaps, we take the estimates of Viste and Gray for MnO_4^-.[52] These give

$$\alpha = -0.262k_0,$$
$$\beta = +0.167k_0, \quad (50)$$
$$\gamma = -0.151k_0,$$

which, with Eq. (45), give

$$\lambda_1 \cong \tfrac{1}{4}N_{T_2}^2(\zeta^d - 0.048k_0^2\zeta^x),$$
$$\lambda_2 \cong \tfrac{1}{4}N_{T_2}N_E(\zeta^d - 0.006k_0^2\zeta^x). \quad (51)$$

These can be further simplified to

$$\lambda_1 \cong \lambda(1-K), \quad \lambda_2 \cong \lambda(1-\tfrac{1}{8}K), \quad (52)$$

with

$$K = 0.048k_0^2\zeta^x/\zeta^d. \quad (53)$$

Here, for simplicity, we have dropped the normalization constants, which, in the analysis to follow, will be found to depart only very slightly from unity.

In this way, we have reduced the problem to a one-parameter (K or k_0) model. We have, in effect, used the group-overlap proportionality and the specific values for MNO_4^- only to estimate the *relative* values of α, β, and γ. The magnitudes of the admixtures are embodied in K, which we will adjust for best fit to the data.

In Fig. 14 we plot the calculated values for D and a, vs K, using Eqs. (29), (31), (33), and (52). Here we have used $E_{JT} = 500$ cm^{-1}, $\Delta = 4500$ cm^{-1}, giving $E_1 = 1500$ cm^{-1}, $E_2 = E_3 = 5500$ cm^{-1}. For λ, we take 57 cm^{-1} and for $\rho_0 = \rho_{10} = \rho_{20} = \rho_{30}$ we take 0.1 cm^{-1}. We see that large changes in D and a are indeed predicted vs K. From Fig. 14, the value of D for ZnTe can be matched at $K = 2.33$. With $\zeta_{Te} = 4136$ cm^{-1},[53] this gives $k_0 = 1.64$, with the corresponding admixture coefficients from (49)

$$\alpha = -0.430, \quad \beta = +0.274, \quad \gamma = -0.248. \quad (54)$$

These, in turn, correspond to

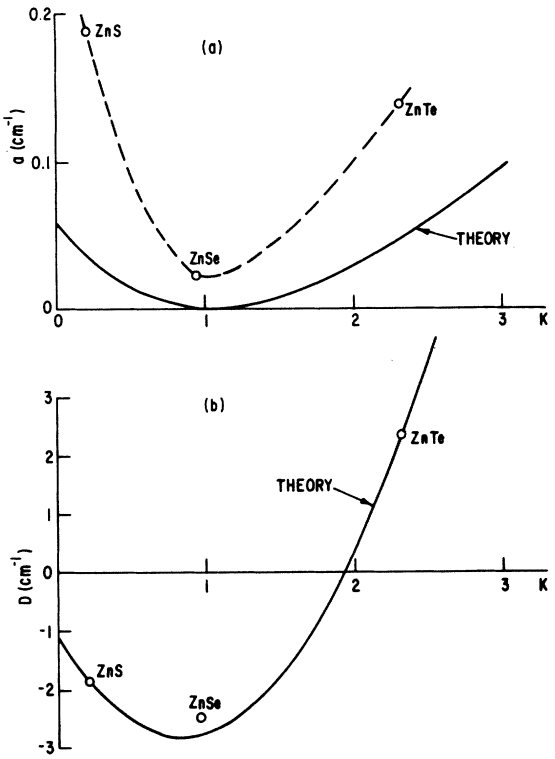

FIG. 14. Calculated fine-structure parameters (a) a, and (b) D, vs ligand parameter K (see text). The experimental points (circles) are plotted at values of K, scaled assuming constant covalency through the series, with the ZnTe value being determined to match the calculated value of D.

$$\alpha^2 N_E^2 = 0.19, \quad (\beta^2+\gamma^2)N_{T_2}^2 = 0.14 \tag{55}$$

fractional ligand admixtures into the ψ_E and ψ_{T_2} wave functions, respectively, values certainly not unreasonable for a covalent tetrahedral environment. For such admixtures, $N_E \sim N_{T_2} \sim 1.02$, justifying their neglect in (52).

In Fig. 14, we have also plotted the values for ZnS and ZnSe. We have plotted them at values of K scaled from the $K=2.33$ value for ZnTe simply by the ratios of the corresponding ligand spin-orbit parameter ζ^x (=1689 cm^{-1} for Se, 382.4 cm^{-1} for S).[53] In doing this we are in effect making the assumption that the admixture coefficients α, β, and γ are roughly constant for the series. This is not strictly true, of course. However, it is probably a reasonable first approximation in that the valence orbital ionization energies[54] of S, Se, and Te are within a few volts of each other, and the degree of covalency should therefore not differ greatly versus ligand. The major part of the variation in K must derive from the order of magnitude change in ζ^x.

From Fig. 14, we see that the ligand-field model accounts quite satisfactorily for the large variation in D. The observed (dashed) line and calculated (solid line) values for a are also given in Fig. 14. Here the calculated values appear uniformly low, but, otherwise, the general trend again is clearly indicated. In particular, the anomolously low value for ZnSe is predicted. From Eq. (33) we see that this reflects the $\lambda_1^2\lambda_2^2$ dependence, λ_1 going to zero and reversing sign at $K \sim 1$. The fact that the predicted values are uniformly low suggests that other contributions, not considered in our fourth-order treatment, may also be important. These could involve excitations to charge-transfer states, higher LS terms, other configurations, etc. Indeed, with such a high order of perturbation theory, such neglected excitations can be expected to become increasingly important. However, we interpret the observed low value of a for ZnSe to indicate that these will also reflect a similar $\sim \lambda_1^n$ dependence. In other words, we interpret these results to reflect the spin-orbit origin of a and the role of the $\langle {}^5\Psi_\xi | \mathcal{H}_{so} | {}^5\Psi_{\xi,\eta} \rangle$ matrix elements in serving as a "bottleneck" for coupling out of the ground ${}^5\Psi_\xi$ state.

B. G shifts

Values calculated for $g_\parallel$ and $g_\perp$ using Eq. (35) are given in Table VI. Here, in order to estimate λ_1 and λ_2, K was first estimated by matching the observed value of D with the curve of Fig. 14. λ_1 and λ_2 were then determined from Eq. (52), and are included in the Table VI. The orbital-reduction factors were determined from Eq. (48) to be

$$k_1 \sim 0.72, \quad k_2 \sim 0.82, \tag{56}$$

using the admixture coefficients of Eq. (54) and the Viste-Gray overlap matrix elements implied by Eq. (50). These were taken as constant for the series, as were $E_1 = 1500$ cm^{-1} and $E_2 = 5500$ cm^{-1}. For the point-ion estimate, $k_1 = k_2 = 1$ and $\lambda_1 = \lambda_2 = 57$ cm^{-1}.

We see that the agreement is satisfactory for $g_\parallel$, but it is poor for $g_\perp$. The ligand-field theory predicts a substantial increase in $g_\perp$ as the ligand goes from S to Se to Te, reflecting the large change in λ_1. This is not observed experimentally, $g_\perp$ being essentially constant.

The reason for this failure is not clear. There are, of course, excitations to charge-transfer states, higher atomic states outside the ${}^5D$ manifold, etc., that have not been specifically included in our treatment, and they may be playing an important role. Their contributions could tend to cancel the anisotropy predicted by (35).

An alternative explanation is that the orbital reduction factor k_1 is smaller than we have estimated. In particular, in Sec. VI A, we have interpreted the good agreement for D and a achieved by the ligand-

TABLE VI. Calculated and observed values of $g_{\parallel}$ and $g_{\perp}$ for the point-ion and ligand-field treatments.

Lattice	K	λ_1 (cm^{-1})	λ_2 (cm^{-1})	$g_{\parallel}$ Theory	$g_{\parallel}$ Expt.	$g_{\perp}$ Theory	$g_{\perp}$ Expt.
Point-ion all ligand-field	0	57	57	1.919		1.926	
CdS	0.2	46	56	1.936	1.93	1.958	1.97
ZnS	0.2	46	56	1.936	1.94	1.958	1.98
ZnSe	1.2	−11	49	1.944	1.96	2.013	1.98
CdTe	2.0	−57	43	1.951	1.98	2.057	1.98
ZnTe	2.3	−74	41	1.954	1.97	2.074	1.99

field model to confirm that the effective spin-orbit interaction $\lambda_1 \vec{L} \cdot \vec{S}$ is being satisfactorily accounted for. A necessary consequence of this is that orbital angular momentum is being induced around the individual atomic cores in the ground $^5B_2$ state. The failure to see a related g shift then would appear to require a weak net *total* angular momentum and a corresponding weak coupling to the external field.

For instance, we may solve for the admixture coefficients (α, β, γ) required to make k_1, Eq. (48), equal to zero. Again maintaining their relative values given by the Viste-Gray overlaps, Eq. (50), we obtain

$$N_{T_2}^2(\beta^2+\gamma^2)=0.52\ , \quad N_E^2\alpha^2=0.65\ . \tag{57}$$

These represent more covalency than was estimated in Sec. VI A, Eq. (55), but they are still not out of line with estimates that have been made for transition elements in tetrahedral environments.[52,55] Such admixtures could still account for λ_1 and λ_2 in Eq. (51) but only if a substantially reduced effective value for ζ^x (~factor of 6 from the free-atom value) were used.

Considering the simplicity of the present ligand treatment, particularly when carried into these largely covalent regimes, this level of agreement is perhaps as good as one can expect. The ligand orbitals we have used, Eq. (42), are highly oversimplified. They do not include $4p$ orbitals on the central ion or valence s orbitals on the ligands, both known to be important[52,55]; nor do they allow for higher excited orbitals or more distant ligand effects. Also, in our treatment we have not allowed for independent adjustment of the admixture coefficients nor have we attempted to estimate reduction of the atomic spin-orbit parameters resulting from ionization state and environmental effects at the ligand sites. Our theory in its present form does demonstrate, however, that reasonable ligand admixtures can account for a large decrease in k_1 as well as the large changes in λ_1. Better agreement than this will evidently require a more sophisticated ligand treatment than we have attemped here.

C. Strain-coupling coefficients

Using Eq. (37), and a computer fit to the data in Fig. 5, the strain-coupling coefficients $c_1, \cdots, c_5$ were determined for the spin Hamiltonian of Cr^{2+} in CdTe. The results are given in Table VII. Also included in Table VII are values calculated from the theory developed in Sec. V B, Eq. (38). For these calculations, we have used $E_1 = 1500\ cm^{-1}$, $E_2 = E_3 = 5200\ cm^{-1}$. For the point-ion estimates, we have taken $\lambda_1 = \lambda_2 = 57\ cm^{-1}$. For the ligand-field estimates, we have taken λ_1 and λ_2 as given by Table VI. For each, however, we have used the *point-ion* estimates for the strain-reduced matrix elements T, U, W as given by Eq. (41).

For the symmetric coefficient c_1 and the tetragonal coefficients c_2 and c_3, the point-ion and ligand-field predictions are identical. For these the agreement with experiment can be considered reasonably satisfactory, the approximate magnitude and the sign of each being accounted for. For the trigonal coefficients c_4 and c_5, however, the wrong sign is predicted in both theories.

The degree of agreement is not unlike that found for other transition-element-ion systems. A good example, is afforded by the d^3 ions, V^{2+}, Cr^{3+}, Mn^{4+}, octahedrally coordinated by oxygen ions, as in MgO and Al_2O_3. For these ions, highly detailed

TABLE VII. Observed and calculated values (cm^{-1}) for the strain coupling coefficients of Cr^{2+} in CdTe.

	Experiment	Theory Point-ion	Theory Ligand-Field
c_1	−2 ± 15	−0.3	−0.2
c_2	+40 ± 15	+6.3	+6.4
c_3	−10 ± 4	−6.1	−6.1
c_4	+40 ± 15	−13.2	−4.6
c_5	+30 ± 10	−15.4	−9.2

calculations have been performed including excitation to other LS terms, configuration interaction, etc.,[56,57] but the agreement with experiment is still only fair.[56–58] These authors have shown that, even in these highly ionic environments, the one-electron strain matrix elements (δ, μ, v, v'), (which bear a direct correspondence to U_1, U_2, W_1, W_2, respectively, in this paper) are only approximately given by a point-ion treatment. As we have found here, they find that the tetragonal coupling coefficients tend to be more reliable. In Al_2O_3, for instance, $v(W_1)$ is of the wrong sign.[58]

The system we are studying here is considerably more complex, having a substantially higher degree of covalency than in the ionic octahedral environments. Our theoretical treatment is also less detailed being restricted to excitations only within the ^5D manifold. At the same time, we are relying in Table VII on point-ion estimates for the strain matrix elements. In view of these, we conclude that the degree of agreement given in Table VII is as good as should be expected. The differences between the point-ion and ligand-field predictions are not great enough to allow a test of the two models, in this case.

Consider c_3 in more detail. From Eq. (38), this is the simplest parameter to interpret, being directly related only to λ_1, E_1, and U_1. Comparing Eqs. (41) and (14), we note that it, in turn, is directly related to the Jahn-Teller tetragonal coupling coefficient V,

$$V = (9/2\sqrt{2}\,R)U_1 = -(3E_1^2/2\sqrt{2}\,R\lambda_1^2)c_3 \,. \tag{58}$$

From the experimental value for c_3 and with $E_1 = 1500\ \mathrm{cm}^{-1}$, $\lambda_1 = -57\ \mathrm{cm}^{-1}$, and $R = 2.78$ Å, this gives $V = -0.33 \pm 0.13$ eV/Å. This is in excellent agreement with the value given in Table IV, which was determined independently from stress *alignment* studies. This would appear to confirm the general consistency of our treatment, both as reflected in the tetragonal-strain coupling coefficient (U_1) within the $^5T_2$ manifold, and the magnitudes of λ_1 and the Jahn-Teller energy. For both V in Table IV and c_3 in Table VII, the theory predicts values ~60% low, presumably reflecting a corresponding underestimate by the point-ion theory of the tetragonal-strain matrix elements.

The stress results for ZnTe, shown in Fig. 11, do not allow analysis for the coupling coefficients, the ⟨110⟩ stress involving both trigonal and tetragonal strain. Additional experiments with stress along a different crystallographic axis would be required for complete analysis. However, the magnitudes of the shifts indicate that the stress-coupling coefficients are comparable to those in CdTe. In ZnS and ZnSe, the lines were broader and reliable measurements versus stress were not possible. We note from Eq. (38) that ZnSe could serve as a critical test for the ligand-field treatment. For it, λ_1 is predicted to be small (see Table VI), and c_3 and c_4 should therefore also be small.

One final test of the theory is afforded by estimating E and θ (Table I), for hexagonal CdS. For CdS, the c/a ratio is 1.6234 compared to 1.6330 for the cubic zinc-blende structure.[26] Therefore, as mentioned in Sec. III B, we may consider the nearest sulfur neighbors as a regular tetrahedron that has been compressed by 0.6% along the [111] axis (c axis). The corresponding strain in terms of the cubic 1, 2, 3 axes (see Fig. 9) is

$$e_{12} = e_{23} = e_{31} = -0.002 \,. \tag{59}$$

For CdS [with $R = 2.52$ Å, $E_1 = 1500\ \mathrm{cm}^{-1}$, $E_{2,3} = 5500\ \mathrm{cm}^{-1}$, and $\lambda_1 = 46\ \mathrm{cm}^{-1}$, $\lambda_2 = 56\ \mathrm{cm}^{-1}$ (Table VI)], Eq. (38) gives

$$c_4 = -12.1\ \mathrm{cm}^{-1}, \quad c_5 = -16.0\ \mathrm{cm}^{-1} \,. \tag{60}$$

Rotating from the cubic 1, 2, 3 axis system to the x, y, z axis system of the defect as shown in Fig. 9, the terms in Eq. (37) resulting from (59) and (60) predict

$$\theta = +1.45^\circ, \quad E = +0.033\ \mathrm{cm}^{-1} \,. \tag{61}$$

These values agree in sign and magnitude with the experimental values, Table I, indicating that here the trigonal coupling coefficients are being satisfactorily accounted for. [Alternatively, the experimental values, Table I, correspond, with Eq. (59), to $c_4 = -16.1\ \mathrm{cm}^{-1}$, $c_5 = -5.1\ \mathrm{cm}^{-1}$, which can be compared with Eq. (60).] This agreement also serves to confirm our interpretation that the Jahn-Teller distortion is essentially a pure tetragonal one, the small departures observed in the spin Hamiltonian being adequately accounted for by the small hexagonal crystal field of the wurtzite lattice.

VII. SUMMARY AND CONCLUSIONS

The EPR results confirm that Cr^{2+} undergoes a static tetragonal distortion in all II-VI lattices studied. Stress-alignment experiments have allowed a direct estimate of the Jahn-Teller coupling coefficients, and these, in turn, have been used to estimate the Jahn-Teller energies. The indicated energies, ~500 cm^{-1}, are consistent with those estimated by Vallin *et al.*[14] from optical studies and serve to confirm their general interpretation of the optical spectra.

A simple point-ion crystal-field model has been found to be incapable of explaining the spin Hamiltonian parameters, and their variations from one crystal to another. A ligand-field model, how-

ever, can account for many of the observed features. In this model, the large variation in the fine-structure splittings, D and a, versus II-VI lattice, is explained by the contribution of the spin-orbit interaction at the ligand cores, which varies substantially as the ligand changes from S to Se to Te. The absence of substantial g shifts is interpreted to indicate significant orbital reduction also accompanying the covalency.

Ligand-field effects have been treated in considerable detail in the literature for transition-element ions in the ionic octahedral environments.[50] The treatment presented here has been similar, but modified as required for the tetrahedral environment. In addition, we have introduced a simple method for including ligand contributions to the spin-orbit interaction with excited d^4 terms. We have found that ligand contributions to these interactions can also be important and that they help to explain the large variation found for a.

The EPR spectrum of Cr^{2+} in II-VI lattices provides a particularly dramatic example of the role of ligand effects in the ground-state spin Hamiltonian. Such effects are often only rather subtle in the much studied octahedrally coordinated sites of ionic crystals.[50] Here they are much more evident both because of the very large spin-orbit interaction associated with the heavier ligands (Se, Te) and because of the increased covalency in the tetrahedrally coordinated II-VI lattices.

Strain-coupling coefficients, describing the changes in the spin Hamiltonian under externally applied stress, have been determined experimentally for Cr^{2+} in CdTe. A simple theory has been developed which includes ligand effects for the spin-orbit interactions but relies on point-ion estimates for the matrix elements of strain. Agreement with experiment is reasonable for the tetragonal coefficients, but the wrong sign is predicted for the trigonal ones. Similar failures are sometimes found for transition-element ions in the more ionic octahedrally coordinated lattices and probably reflect the failure of the point-ion approximations to the strain matrix elements.

The ligand-field treatment developed in this paper is a very simple one. It does not include the effect of excitations to charge-transfer states, for instance. Such excitations have been demonstrated to give important contributions to g shifts where covalency is important.[59] Simple estimates of their possible contribution to D indicate that their effects in this case may be relatively smaller.[60] However, it is still difficult to rule out their importance. The main justification for not attempting to include them is that most of the essential features of the spin Hamiltonian appear to be describable without them. Clearly, detailed agreement would require their inclusion.

ACKNOWLEDGMENTS

The authors acknowledge the helpful assistance of L. A. Gruenke in all phases of the experiments. The authors thank W. W. Piper for the use of the 14-GHz EPR spectrometer and superconducting magnet. They are grateful to D. R. Locker, H. H. Woodbury, J. S. Prener, R. K. Swank, and M. Aven for supplying the crystals used in this study. The authors are particularly indebted to F. S. Ham for several helpful discussions and a critical reading of the manuscript. Helpful discussions with R. P. Messmer are also gratefully acknowledged. Travel grants from the Swedish Natural Science Research Council's Committee of Solid State Physics (G.D.W.) and from Wallenbergs Stiftelse (J.T.V.) are gratefully acknowledged.

APPENDIX

As shown by Trees,[45] spin-orbit coupling between the ground and higher LS terms of a given configuration provides an additional important interaction having exactly the same form as Eq. (25). In this appendix we will demonstrate the procedure we have followed to estimate these additional contributions to ρ_1, ρ_2, and ρ_3.

As an example, we will outline the calculation for ρ_2. From Eq. (25), a typical matrix element within the ^5D manifold of the spin-spin Hamiltonian is

$$\langle {}^5\Psi_\theta,\ M_s=0\,|\,\mathcal{H}_{ss}\,|\,{}^5\Psi_\xi,\ M_s=2\rangle = -3\sqrt{2}\,i\rho_2\ . \tag{A1}$$

Spin-orbit coupling to excited triplet states also produces an effective matrix element between these states which, to second order in the spin-orbit interaction, can be written

$$\langle {}^5\Psi_\theta,\ M_s=0\,|\,\Theta\,|\,{}^5\Psi_\xi,\ M_s=2\rangle\ , \tag{A2}$$

where

$$\Theta=\sum_n \frac{\mathcal{H}_{so}\,|\,n\rangle\langle n\,|\,\mathcal{H}_{so}}{E_0-E_n}\ . \tag{A3}$$

Here n is summed over all excited triplet states within the d^4 manifold.

For the free ion, the excited d^4 triplet states are ~20 000 cm^{-1} above the ground ^5D state,[46] an energy splitting significantly larger than the crystal-field splittings in the ^5D state (~5000 cm^{-1}). As a first approximation, therefore, we will consider $|E_0-E_n|$ to be constant ($=E$) and take it from under the summation sign:

$$\Theta\cong -(1/E)\sum_n \mathcal{H}_{so}\,|\,n\rangle\langle n\,|\,\mathcal{H}_{so}\ . \tag{A4}$$

Invoking closure, this may now be written

$$\Theta=-(1/E)\left(\mathcal{H}_{so}^2-\sum_m \mathcal{H}_{so}\,|\,m\rangle\langle m\,|\,\mathcal{H}_{so}\right), \tag{A5}$$

where m is now conveniently summed only over the ground-state quintet orbitals.

To evaluate the matrix elements of (A2) and (A5), we first express the quintet wave functions as products of the one-electron wave functions, e.g.,

$$
\begin{aligned}
&{}^5\Psi_\zeta(M_s=2)=(\theta\epsilon\xi\eta)\ ,\\
&{}^5\Psi_\eta(M_s=1)=\tfrac{1}{2}[(\bar{\theta}\epsilon\xi\zeta)+(\theta\bar{\epsilon}\xi\zeta)\\
&\qquad\qquad+(\theta\epsilon\bar{\xi}\zeta)+(\theta\epsilon\xi\bar{\zeta})]\ , \qquad\qquad \text{(A6)}\\
&{}^5\Psi_\theta(M_s=0)=(1/\sqrt{6})[(\bar{\epsilon}\bar{\xi}\eta\zeta)+(\bar{\epsilon}\xi\bar{\eta}\zeta)\\
&\qquad\qquad+(\bar{\epsilon}\xi\eta\bar{\zeta})+(\epsilon\bar{\xi}\bar{\eta}\zeta)+(\epsilon\bar{\xi}\eta\bar{\zeta})+(\epsilon\xi\bar{\eta}\bar{\zeta})]\ ,
\end{aligned}
$$

etc. Here $(\theta\epsilon\xi\eta)$ is a Slater determinant of the one-electron orbitals ψ_θ, ψ_ϵ, ψ_ξ, and ψ_η with all electrons having $m_s=+\frac{1}{2}$. The bar denotes $m_s=-\frac{1}{2}$. We then evaluate all relevant matrix elements in (A5) of the spin-orbit interaction

$$\mathcal{H}_{so}=\sum_i \xi\vec{l}_i\cdot\vec{s}_i\ . \qquad \text{(A7)}$$

For instance,

$$
\begin{aligned}
\sum_i \xi l_{xi}s_{xi}\,|\,{}^5\Psi_\zeta, M_s=2\rangle &= \tfrac{1}{2}\xi_2[-i\sqrt{3}\,(\bar{\xi}\epsilon\xi\nu)\\
&\quad -i(\theta\bar{\xi}\xi\eta)+i(\theta\epsilon\bar{\epsilon}\eta)+i\sqrt{3}\,(\theta\epsilon\bar{\theta}\eta)]-i\zeta_1(\theta\epsilon\xi\bar{\zeta})\ ,
\end{aligned}
$$

leading to

$$\langle{}^5\Psi_\eta, M_s=1\,|\sum_i \xi l_{xi}s_{xi}\,|\,{}^5\Psi_\zeta, M_s=2\rangle=-\tfrac{1}{4}i\xi_i\ .$$

Here we have used the properties of the one-electron operators

$$
\begin{aligned}
&l_x\theta=-i\sqrt{3}\,\xi\ ,\\
&l_x\epsilon=-i\xi\ ,\\
&l_x\xi=i(\epsilon+\sqrt{3}\,\theta),\\
&l_x\eta=-i\zeta\ ,\\
&s_x\theta=\tfrac{1}{2}\bar{\theta}\ ,
\end{aligned}
$$

etc. Evaluating all nonzero matrix elements of (A5) in similar fashion leads to

$$\langle{}^5\Psi_\theta, M_s=0\,|\,\mathcal{O}\,|\,{}^5\Psi_\zeta, M_s=2\rangle=-(5i/8\sqrt{2}\,E)\xi_1\xi_2\ . \qquad \text{(A8)}$$

With (A1), this gives

$$\rho_2=(5/48E)\xi_1\xi_2=(5/3E)\lambda_1\lambda_2\ .$$

---

*Present address: Dept. of Physics, Chalmers Technical University, Gothenburg, Sweden.

[1] P. B. Dorain and D. Locker, Bull. Am. Phys. Soc. 1, 306 (1962).

[2] T. L. Estle, G. K. Walters, and M. deWit, in *Paramagnetic Resonance*, edited by W. Low (Academic, New York, 1963), Vol. 1, p. 144.

[3] K. Morigaki, J. Phys. Soc. Jap. 18, 733 (1963).

[4] K. Morigaki, J. Phys. Soc. Jap. 19, 187 (1964).

[5] G. R. Wagner and J. G. Castle, Bull. Am. Phys. Soc. 11, 906 (1966).

[6] D. C. Look and D. R. Locker, Bull. Am. Phys. Soc. 14, 835 (1969).

[7] D. R. Locker and P. B. Dorain, Bull. Am. Phys. Soc. 15, 249 (1970).

[8] J. T. Vallin and G. D. Watkins, Phys. Lett. A 37, 297 (1971).

[9] G. R. Wagner, J. Murphy, and J. G. Castle, Jr., final report ARL 70-0108, Aerospace Research Laboratories, Contract No. AF33 (615)-3579, June, 1970 (unpublished). Available from Clearinghouse, U.S. Dept. of Commerce, Springfield, Va. 22151.

[10] M. deWit, A. R. Reinberg, W. C. Holton, and T. L. Estle, Bull. Am. Phys. Soc. 10, 329 (1965).

[11] T. L. Estle and W. C. Holton, Phys. Rev. 150, 159 (1966).

[12] Dorain and Locker (Refs. 1 and 7), originally concluded that Cr^{2+} was interstitial in CdS. They have subsequently reinterpreted their results and in the oral presentation of Ref. 7 also concluded it to be substitutional.

[13] J. T. Vallin, G. A. Slack, S. Roberts, and A. E. Hughes, Solid State Commun. 7, 1211 (1969).

[14] J. T. Vallin, G. A. Slack, S. Roberts, and A. E. Hughes, Phys. Rev. B 2, 4313 (1970).

[15] C. S. Kelley and F. E. Williams, Phys. Rev. B 2, 3 (1970).

[16] J. M. Langer and J. M. Baranowski, Phys. Status Solidi 49, 499 (1972).

[17] P. A. Slodowy and J. M. Baranowski, Phys. Status Solidi 44, 155 (1971).

[18] E. M. Wray and J. W. Allen, J. Phys. C 4, 512 (1971).

[19] H. Nelkowski and G. Grebe, J. Lumin. 1, 88 (1970).

[20] J. T. Vallin and G. D. Watkins, Solid State Commun. 9, 953 (1971).

[21] G. D. Watkins and F. S. Ham, Phys. Rev. B 1, 4071 (1970).

[22] G. D. Watkins and J. W. Corbett, Phys. Rev. 121, 1001 (1961).

[23] This result can be deduced directly from the symmetry of the defect, D_{2d}.

[24] D. Belincourt, H. Jaffe, and L. R. Shiozawa, Phys. Rev. 129, 1009 (1963).

[25] Experience in other systems [G. D. Watkins and J. W. Corbett, Phys. Rev. 134, A1359 (1964); Phys. Rev. 138, A543 (1965); and E. L. Elkin and G. D. Watkins, Phys. Rev. 174, 881 (1968)] has shown that this simple procedure often reproduces T_2 rather well.

[26] W. L. Roth, in *Physics and Chemistry of II-VI Compounds*, edited by M. Aven and J. S. Prener (North-Holland, Amsterdam, 1967), p. 117.

[27] The hexagonal ZnS was grown synthetically by Eagle-Pitcher Co. It is possible that the crystal is actually predominantly cubic but with a preferential ⟨111⟩ stacking-fault axis.

[28] A. E. Hughes and J. T. Vallin (unpublished).

[29] M. T. Hutchins, in *Solid State Physics*, edited by F. Seitz and D. Turnbull (Academic, New York, 1963), Vol. 16, p. 227.

[30] M. D. Sturge in *Solid State Physics*, edited by F. Seitz, D. Turnbull, and H. Ehrenreich (Academic, New York,

1967), Vol. 20, p. 91.
[31]F. S. Ham, in *Electron Paramagnetic Resonance*, edited by S. Geschwind (Plenum, New York, 1972), p. 1.
[32]V. Opik and M. H. L. Pryce, Proc. R. Soc. A 238, 425 (1957).
[33]θ and ϵ are used to designate partner functions (or operators) belonging to the irreducible representation E of T_d and transforming, respectively, as $z^2-\frac{1}{2}(x^2+y^2)$ and $\frac{1}{2}\sqrt{3}(x^2-y^2)$, while ξ, η, and ζ designate those belonging to T_2 and transforming, respectively, as yz, zx, and xy.
[34]The irreducible representations of D_{2d} are labeled with carets.
[35]The $^5D(d^4)$ state is equivalent to a single d hole. These expressions also hold for a single d electron if the sign is reversed.
[36]B. Nygren, J. T. Vallin, and G. A. Slack, Solid State Commun. 11, 35 (1972).
[37]B. Nygren, J. T. Vallin, and J. M. Baranowski (unpublished).
[38]The fact that alignment is observed for ZnSe means, however, that the applied strain exceeds the internal strain. With this as a guide, a rough estimate can be made from Fig. 4 of the internal strain $\langle e_\theta^2+e_\epsilon^2\rangle^{1/2}\sim 5\times 10^{-5}$. This is generally consistent with the observed linewidths. For ZnS the internal strain must be a factor of ~ 3 larger in order to explain the small stress-induced alignment observed there.
[39]The origin of this jump is not understood but may be associated with subtle line-shape changes under stress. The spectra were less intense here, which required monitoring the peak-peak amplitudes of the derivative line shapes rather than the integrated areas. Although no substantial broadening was apparent on the lines studied, minor changes in line shape could change the relationship between the peak-peak derivative amplitude and the integrated area, producing such an effect.
[40]We will take $q_L=-2e$ for all of the point-ion calculations in this paper.
[41]A. Abragam and B. Bleaney, *Electron Paramagnetic Resonance of Transition Ions* (Oxford U. P., London, 1970), p. 399.
[42]See, for example, G. D. Watkins and J. W. Corbett, Phys. Rev. 134, A1359 (1964).
[43]Reference 41, pp. 593 and 678.
[44]M. Tinkham, *Group Theory and Quantum Mechanics* (McGraw-Hill, New York, 1964), p. 131.
[45]R. E. Trees, Phys. Rev. 82, 683 (1951).
[46]*Atomic Energy Levels*, edited by C. E. Moore, Natl. Bur. Std. Circ. No. 467 (U. S. GPO, Washington, D. C., 1949). This is an average over the d^4 triplet free-ion terms.
[47]M. H. L. Pryce, Phys. Rev. 80, 1107 (1950).
[48]R. E. Watson and M. Blume, Phys. Rev. 139, A1209 (1965).
[49]F. S. Ham (private communication).
[50]J. Owen and J. H. M. Thornley, Rep. Prog. Phys. 29, 675 (1966).
[51]M. Wolfsberg and L. Helmholtz, J. Chem. Phys. 20, 837 (1952).
[52]A. Viste and H. B. Gray, Inorg. Chem. 3, 1113 (1964).
[53]R. G. Barnes and W. V. Smith, Phys. Rev. 93, 95 (1954). The one-electron spin-orbit parameter is two-thirds the fine-structure splitting, listed in Table II of this reference.
[54]C. J. Ballhausen and H. B. Gray, *Molecular Orbital Theory* (Benjamin, New York, 1965), p. 122.
[55]J. P. Dahl and C. J. Ballhausen, in *Advances in Quantum Chemistry*, edited by P. Löwdin (Academic, New York, 1968), Vol. 4, p. 170.
[56]R. M. Macfarlane, J. Chem. Phys. 47, 2006 (1967).
[57]R. M. Macfarlane, Phys. Rev. 158, 252 (1967).
[58]Elsa Feher and M. D. Sturge, Phys. Rev. 172, 244 (1968).
[59]I. Fidone and K. W. H. Stevens, Proc. Phys. Soc. Lond. 73, 116 (1959).
[60]G. D. Watkins (unpublished).